Cluster-Based Milling Method
for Large-Field-of-View
Volume Electron Microscopy

Maria Kormacheva

München 2023

Cluster-Based Milling Method for Large-Field-of-View Volume Electron Microscopy

Maria Kormacheva

Dissertation
der Fakultät für Physik
der Ludwig-Maximilians-Universität
München

vorgelegt von
Maria Kormacheva
aus Severodvinsk, Russland

München, den 03.05.2023

Contents

List of Figures

List of Tables

Abstract

Current methods for automated volume image acquisition that allow resolving the structure of neural circuits have a limited field-of-view. This work investigates using a gas cluster ion beam (GCIB) to overcome the field-of-view limitation and explores the combination with a multi-beam scanning electron microscope (mSEM) to create a system for the acquisition of the whole mouse brain.

To this end, a staining protocol for $500\,\mu m$ thick whole-coronal cross-sections is established, and a GCIB is incorporated with a scanning electron microscope (SEM) to identify optimal system parameters. In addition, an electron beam irradiation system is built and automated to induce conductivity in collected sections for SEM imaging.

The results verify that ion milling can keep up with the imaging rate in the mSEM while maintaining adequate quality. In addition, software is implemented for targeted image acquisition in the mSEM. Finally, calculations show that acquiring the whole mouse brain is feasible but heavily dependent on the imaging rate and the number of parallel GCIB-mSEM systems.

Zusammenfassung

In dem Feld der Konnektomik werden mittels Rasterelektronenmikroskopie aufeinanderfolgende Bilder eines Gehirnausschnitts aufgenommen, die dann anschließend zu einem Volumen zusammengesetzt werden können. Dadurch können neuronale Schaltkreise mit der Auflösung einzelner Synapsen im dreidimensionalen Raum untersucht werden. Die derzeitigen Methoden zur automatisierten Aufnahme dieser Bilder, haben allerdings nur ein begrenztes Sichtfeld. Um dieses zu erweitern, wird in dieser Arbeit die Verwendung eines Gascluster-Ionenstrahls (GCIB) in Kombination mit einem Mehrstrahl- Rasterelektronenmikroskop (mSEM) erprobt, um ein System für die Erfassung des gesamten Mausgehirns zu schaffen.

Zu diesem Zweck wird ein Protokoll für die Färbung mit Schwermetallen für dicke, ganze koronale Querschnitte erstellt. Um optimale Systemparameter zu ermitteln, wird zusätzlich ein GCIB mit einem Rasterelektronenmikroskop (SEM) kombiniert. Darüber hinaus wird ein Elektronenstrahl-Bestrahlungssystem gebaut und automatisiert, um Leitfähigkeit in den gesammelten Schnitten für die SEM-Bildgebung zu induzieren. Zudem wird eine Software für die Bildaufnahme im mSEM implementiert.

Dies beinhaltet zusätzlich 1) das Erstellen eines Protokolls für die Schwermetallfärbung dicker $500\,\mu m$, ganzer koronaler Querschnitte eines Mäusegehirns; 2) die Kombination eines GCIB mit einem Rasterelektronemikroskop (SEM) zur Ermittlung optimaler Systemparameter; 3) Bau und Automatisierung eines Elektronenstrahl-Bestrahlungssystems zur Induktion der Leitfähigkeit in den gesammelten Schnitten und 4) Implementierung einer Software für die gezielte Bildaufnahme im mSEM.

Die Ergebnisse belegen, dass die Verwendung des GCIB mit der Abbildungsrate im mSEM mithalten kann und dabei eine angemessene Qualität beibehalten wird. Schließlich zeigen Berechnungen, dass die Aufnahme des gesamten Mausgehirns mit diesem System machbar ist, aber stark von der Bildgebungsrate und der Anzahl der parallelen GCIB-mSEM-Systeme abhängt.

Chapter 1

Introduction

> The greatest challenge in all of science
> is to understand how the mysteries of
> human nature ... arise from the
> physical matter of the brain.
>
> ———————————————————
> Eric R. Kandel, *The Disordered Mind*

Since the birth of humanity, curiosity has abounded around the origin of the impulses that rule the human body. As early as the 5th century BC the ancient Greek philosopher Alcmaeon suggested that it is the brain, and not the heart, that controls the body (Doty, 2007). In the 4th century BC, Praxagoras, a Greek physician and philosopher, postulated that "there were minuscule arteries responsible for transmitting signals through the body, and some arteries becoming so thin at their endings that their lumen virtually disappeared" (Panegyres & Panegyres, 2016). For those narrow arteries, he used the word 'neuron' - the Greek word for 'cord' - that later entered the vocabulary of biologists to denote the cells of the nervous system. However, it was not until 1837 AD that the first neuron was located and described by Czech physiologist Jan Evangelista Purkinje (Purkinje, 1838). It was the largest cell in the cerebellum, later named after him.

With the invention of the optical microscope, studies of the brain became more sophisticated, but neurons were still challenging to identify and, hence, to study. A breakthrough technology developed by Camillo Golgi (Finger, 1994) allowed staining of neurons in its entirety including its axon and dendrite branches, making them visible in an optical microscope for the first time. The staining permitted Santiago Ramón y Cajal to study neurons, granting us a great legacy of his illustrious notes (Swanson et al., 2017), which present

Cajal not only as a careful observer but also as an accomplished artist. The myriad illustrations of cells of different shapes, forms, and sizes show us the wide variety of neurons in mammals' brains. One hundred years later, the total number of cell types in the human brain is still debated. Except for this notorious organ, the structure of all other organ systems in our body and the relation of their structure to the their function is now pretty much known. The brain is the only organ for which scientists seriously consider imaging the entire organ's volume with the hope of coming closer to understanding its functioning (Lichtman & Denk, 2011).

Connectomics

The invention of the transmission electron microscope (TEM) (Knoll & Ruska, 1932) in the first half of the 20th century was the next major technological breakthrough in the history of neuroanatomy. Electrons make it possible to image tissue, including neural tissue, at a much higher resolution than photons and allow to unambiguously identify neurons, junctions between neurons - called 'synapses', and other cellular structures. These advances inspired neuroscientists to create a detailed map of all neuronal connections in the brain at a synaptic resolution — *connectome* — by acquiring a volume of tissue. Volume acquisition methods involve thousands of iterations of sequential sectioning and imaging with the variation typically lying in the means of sectioning: the tissue layer can either be sectioned with a knife or removed by ion beam milling.

Biological materials, among which is the brain, consist largely of molecules containing hydrogen, carbon, oxygen and nitrogen — molecules with a low atomic weight. Therefore, it is difficult to differentiate among the electron opacity of various cell components, moreover, such differentiation is rendered even more difficult when a specimen is embedded in an organic epoxy resin, that also consists of the same molecules. Hence, in order to determine the shape and location of cell components, the application of selective heavy metal staining is necessary.

Over the years, the scanning electron microscope (SEM) (von Ardenne, 1938) has caught up with TEM in terms of resolution and even increased the size of area that can be imaged. Additionally, SEM makes automated volume acquisition possible. This has led to the development of new SEM-based approaches Table 1.1. A necessary condition for imaging in the SEM is elimination of sample surface charging.

Methods of Connectomics

In serial block-face SEM a diamond knife ultramicrotome is placed inside the vacuum chamber of a microscope (DiK-SEM) (Denk & Horstmann, 2004). The top layer of the tissue block is imaged before being cut away with the knife to expose the next. Due to lack of conductivity in the block this method requires charge elimination techniques. Furthermore, this block-face SEM method is destructive, as the sections are lost as soon as they are removed from the surface. Alternatively, thin sections can be cut in a water bath and automatically picked up on a conductive tape to be imaged later in SEM (ATUM-SEM) (Hayworth et al., 2006), permitting wider and longer sections to be imaged. Due to the nature of thin sections and imaging in SEM on a conductive substrate, this method does not require additional steps to eliminate charging.

The tissue layer can also be removed by ion beam milling. One example is focused ion beam SEM (FIB-SEM) (Langford, 2006; Knott et al., 2008). This method has a superior z-axis resolution compared to the mechanical removal of sectioning with a diamond knife; however, it has a fundamental physical limitation in that the ion beam can only be tightly focused over a short distance, capping imaging volumes. Another milling method - gas cluster ion beam SEM (GCIB-SEM) (Hayworth et al., 2020) lifts the constraints on the lateral surface area that can be imaged, keeping high z-resolution. Like the block-face SEM method, ion beam milling methods are destructive, creating demand for almost perfect reliability. The proposed approach involves cutting a block into several thick sections before submilling them with the GCIB between imaging cycles. To deal with the charging problem in the SEM, the authors introduced high density electron irradiation to induce conductivity in the sections.

Both TEM and SEM are equally used to reconstruct neural circuits. The first organism's brain to be deciphered was *Caenorhabditis elegans* — a transparent roundworm only 1 mm in length with a very small and simple nervous system (White et al., 1986). The team cut the stained and embedded worm into thousands of thin sections, imaged each section using TEM, and manually followed the neural processes to obtain the worm's complete neural circuitry. It took scientists 14 years to acquire and analyse the connections of the 302 neurons of the worm's brain.

The DiK-SEM technology was applied to obtain the whole volume of the spinal cord of a larval zebrafish, *Danio rerio*, in order to gain a mechanistic understanding of motoneuron (Svara, 2017) and to obtain the HVC and Area X of zebrafinch, *Taeniopygia guttata*, to test anatomical hypotheses about their synaptic connectivity (Kornfeld, 2017).

Method	Z-resolution	Surface area	Use of block/sections
DiK-SEM	20 nm [1]	166 µm × 166 µm [5]	cutting the whole block
ATUM-SEM	30 nm [2]	2.5 mm × 6 mm	thin sectioning in water bath
FIB-SEM	<10 nm [3]	20 µm × 300 µm [3]	no knife sectioning
GCIB-SEM	<110 nm [4]	> 10 mm [4]	semi-thick sectioning

Table 1.1: Comparison of the volume SEM methods.

1 - Denk & Horstmann (2004)
2 - Briggman & Bock (2012)
3 - Scheffer et al. (2020)
4 - Hayworth et al. (2020)
5 - Kornfeld et al. (2017)

Recently, a team of scientists from HHMI Janelia Research Campus obtained a complete EM volume of the brain of an adult *Drosophila melanogaster* (Zheng et al., 2018) — a tiny annoying fly that buzzes around ripe fruits. The brain was, again, cut into thousands of thin sections that were imaged using TEM. The reconstruction and analysis of this connectome is still in progress.

Challenges of the Large Volume Connectomics

With these advances, the next milestone in connectomics is a mouse or small bird brain. This, however, is not as simple as it seems. First and foremost, a reliable and uniform staining method with heavy metals for the whole mouse brain is necessary to provide membrane contrast in SEM.

Moreover, uninterrupted imaging with a single beam at synaptic resolution would require more than 12 000 yr assuming a mouse brain volume of approximately $V = 10\,\text{mm} \times 10\,\text{mm} \times 10\,\text{mm}$ imaged at $z = 10\,\text{nm}$ intervals with an image acquisition rate of $f = 2.5\,\text{MHz}$ and a pixel resolution of $p = 10\,\text{nm} \times 10\,\text{nm}$.:

$$t_{img} = \frac{V}{z \cdot N_{beams} \cdot f \cdot p} = \frac{10\,\text{mm} \cdot 10\,\text{mm} \cdot 10\,\text{mm}}{10\,\text{nm} \cdot 1 \cdot 2.5\,\text{MHz} \cdot 10\,\text{nm} \cdot 10\,\text{nm}} \approx 12\,676\,\text{yr}. \qquad (1.1)$$

Contrast plays a crucial role in imaging speed: the higher the contrast, the faster the supported imaging rate. Better staining protocols, that allow image acquisition at

$f = 20\,\mathrm{MHz}$, can shorten the acquisition time to $\approx 1584\,\mathrm{yr}$. These calculations, however, do not take into account the additional time required for moving the samples to different imaging locations, the cutting/milling between the imaging cycles, the transfer of the sample between imaging and cutting/milling, sample preparation and machine maintenance.

Scanning Electron Microscopy

Electron microscopy analysis is built on the effects of elastic and inelastic scattering of an incident electron beam on a specimen's atoms. Elastic collision produces back-scattered electrons (BSEs) that come from deep regions of the sample (Figure 1.1). Heavy elements — with high atomic numbers — back-scatter electrons more strongly than light elements. Inelastic scattering produces emission of secondary electrons (SEs). A single incident electron can produce several SEs. Secondary electrons may be produced during the initial interaction between incident electrons and the surface atoms (SE1) or via back-scattered electrons (SE2) (Figure 1.1). Due to their low energy, only SE originating closer to the surface have a chance of escaping the surface, resulting in surface topography contrast. When the block surface is devoid of topographic features, the surface topography contrast is negligible and all measured contrast comes from the specimen composition. The scanning electron microscope generates an image by scanning a focused electron beam across the sample's surface and detecting these types of electrons. Combining the intensity of the detected signal with the beam's position produces an image — electron micrograph.

Along with the advances in methods for volume sectioning of biological tissue, imaging has also shown significant improvement. Now, not just one but mul-
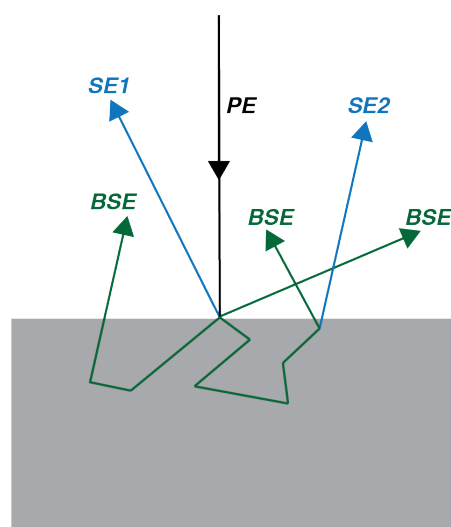
Figure 1.1: Electrons produced by primary electron (PE) beam scanning a tissue. Possible detected outcomes of the interaction with the tissue are back-scattered electrons (BSE) from within the sample and secondary electrons (SE) from the region close to the surface. SE1 are produced by the initial interaction of the PE with the surface atoms and SE2 — by the back-scattered electrons.

tiple electron beams (mSEM) in a single column make it possible to detect SE1 with an In-lens detector in parallel (Eberle et al., 2015) — a development that makes image acquisition almost 100 times faster. With this quicker image acquisition rate, the whole mouse brain imaged with $p = 10\,\text{nm} \times 10\,\text{nm}$ pixel size and $f = 2.5\,\text{MHz}$ acquisition rate can be acquired within:

$$t_{img} = \frac{S}{N_{beams} \cdot f \cdot p} = \frac{10^8 \,\text{mm}}{91 \cdot 2.5\,\text{MHz} \cdot 10\,\text{nm} \cdot 10\,\text{nm}} \approx 140\,\text{yr.} \qquad (1.2)$$

Again, considering a sample with higher contrast, increasing image acquisition rate to $f = 20\,\text{MHz}$ would shorten the acquisition time to $\approx 18\,\text{yr}$. These improvements makes the acquisition of large volumes such as a mouse brain seem increasingly feasible.

Objectives

The work described in this thesis aims to explore and develop a reliable method for acquiring large volumes of biological tissue within a feasible amount of time. Such a method is necessary if one wants to obtain a connectome of a mouse or a small bird brain. Table 1.1 summarises the abilities of the four SEM-based volume methods and shows that GCIB milling currently provides the best possible match for large volume SEM methods to use in conjunction with mSEM. Therefore, we set the goal to explore this technology in conjunction with mSEM imaging and establish a pipeline for large field of view acquisition exploiting the combination of the two.

Cutting the desired volume into many sections, collecting them on multiple wafers and then submilling them with GCIB allows for parallelising the acquisition: while one of the wafers with samples is imaged, the other one is milled. Ideally, these processes happen at the same rate, the system is automated and the preparatory procedure does not delay the whole acquisition.

Thus, the ideal milling time for a 2-inch wafer ($R = 25.4\,\text{mm}$) that is fully covered with slices should not exceed the estimated imaging time with $p = 10\,\text{nm} \times 10\,\text{nm}$ pixel size and $f = 2.5\,\text{MHz}$ acquisition rate:

$$t_{img} = \frac{\pi \cdot R^2}{N_{beams} \cdot f \cdot p} = \frac{\pi \cdot 25.4\,\text{mm} \cdot 25.4\,\text{mm}}{91 \cdot 2.5\,\text{MHz} \cdot 10\,\text{nm} \cdot 10\,\text{nm}} \approx 24\,\text{h}. \tag{1.3}$$

Moreover, volume acquisition can be done not only in a single GCIB-mSEM machine, but distributed across multiple, further decreasing the necessary time for acquiring the whole mouse brain calculated in Equation 1.2.

Our suggested pipeline is shown in Figure 1.2. The tissue is stained with heavy metal and embedded in epoxy resin (not shown in the figure), then the tissue block is cut in a water bath and the sections are collected on a 2-inch wafer. Next, the wafer with samples is irradiated under an electron beam to make the sections conductive. The iteration between image acquisition and ion beam milling starts with imaging the surface in the mSEM. The stage in our standard 91 beam mSEM was upgraded to hold a specially designed piezo stage. This stage is lighter and require less time to settle after a movement, allowing for quicker acquisition of nearby locations decreasing total imaging time.

This introductory chapter provided an overview of connectomics and justified the need for a method for large-volume SEM. chapter 2 covers sample preparation for large field of view SEM. chapter 3 presents a procedure for collecting thick sections cut with an
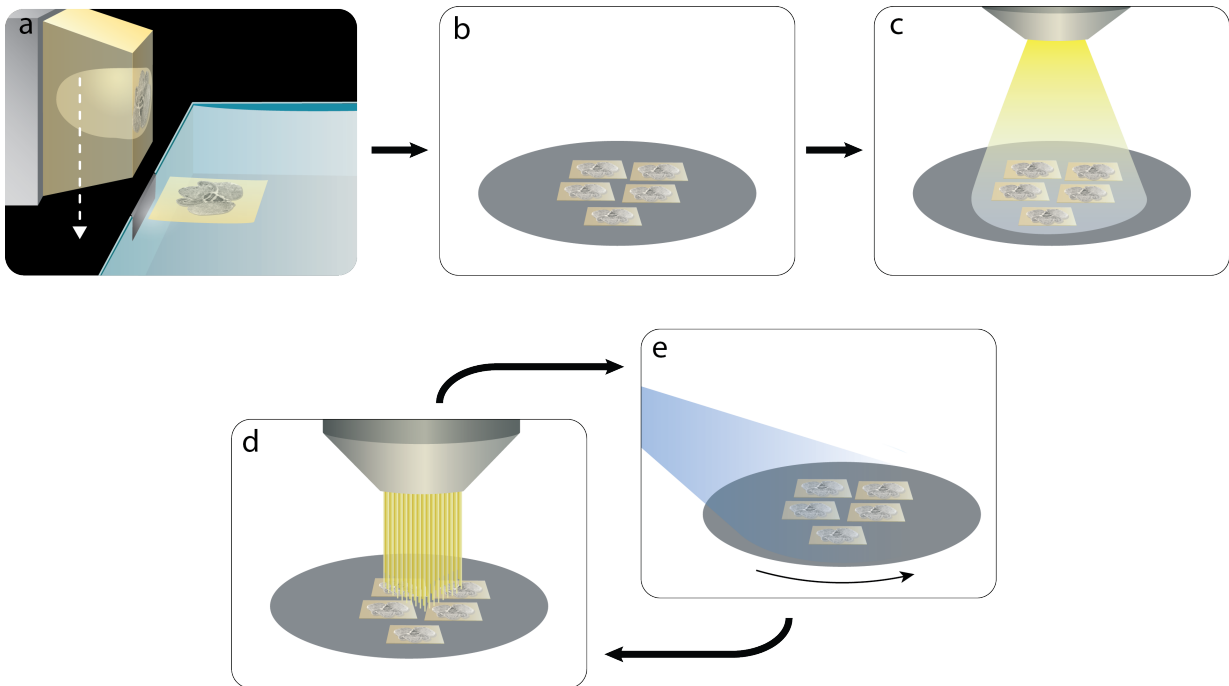
Figure 1.2: Schematic of the GCIB-mSEM pipeline. (a) A heavy metal stained sample that is embedded in epoxy resin is cut in a water bath, and (b) the sections are collected on a 2-inch wafer, then (c) the wafer with samples is irradiated under an electron beam to make them conductive, after that the acquisition iterations start with (d) imaging in the mSEM and is followed by (e) GCIB milling to expose the next layer of the volume for imaging.

ultramicrotome and preparing tissue for imaging in the mSEM. chapter 4 describes a design for a system to induce conductivity of the samples. chapter 5 explores the possibilities of the gas cluster ion beam. The final chapter 6 summarises the results and discusses the directions for future work.

Chapter 2

Tissue Preparation

Electron microscopy is the instrument for imaging biological tissue at nanometre resolution and identifying cells, their organells and connections to build a detailed map. To deliver sufficient contrast and resolution to identify synapses and follow all neural wires reliably, electron microscopy requires careful preparation of the specimen for optimal preservation of the structural information that is needed for the reconstruction of the circuits. An electron micrograph is an image of an altered specimen, different from its living state, and the alteration heavily depends on the preparatory procedure used.

The GCIB-mSEM method, though initially tested on relatively small samples (Hayworth et al., 2020), is ready to accept the challenge of a large volume specimen. The method for the preparation of brain tissue of a large volume for electron microscopy is the BROPA protocol (Mikula & Denk, 2015). Unfortunately, the protocol requires a lot of time to prepare the tissue and largely vary in its results, a phenomenon not yet understood. Therefore, there was first a need for a preparation technique of a large surface tissue to test the capabilities of the GCIB-mSEM system.

This chapter details the fundamentals of sample preparation and tackles the challenge of preparing whole coronal cross-section slices of a mouse brain that have cell component contrast in SEM secondary electron imaging. There were three major challenges in producing a sample: (1) uniform staining, (2) high tissue contrast in mSEM and (3) smooth sectioning.

2.1 Introduction

The basic preparation of a biological specimen for imaging in an SEM consists of three steps. First, the tissue is chemically fixed to avoid large variations from its living state and to preserve as much information as possible. Second, the tissue block needs impregnation with heavy metals to reflect the preserved information and have an excellent tissue contrast to resolve this information on a micrograph. Third, the stained tissue needs to be embedded in epoxy resin to provide stability to the fragile, heavy metal stained tissue.

Fixation

Besides its ability to stabilise cellular components of biological tissue, tissue fixation also protects the specimen against consequent exposure to toxic substances that are part of EM preparation. An ideal fixative should kill the specimen quickly, causing minimum damage to the fine structure. Though none of the commonly used fixative components - formaldehyde and glutaraldehyde - are ideal. Formaldehyde is the smallest and simplest aldehyde; it penetrates rapidly into the tissue owing to its size but does not strongly cross-link the tissue and can be easily washed out with aqueous solutions. Glutaraldehyde, on the other hand, is a relatively large molecule. Hence it penetrates tissue slower than formaldehyde but provides strong, virtually irreversible cross-linking (Sabatini et al., 1963). A buffer is needed to maintain the physiological pH(7.4) to keep the fine structure when using glutaraldehyde as a fixative. Cacodylate buffer is one of the most commonly used buffering materials for brain tissue preservation, as it is effective at pH7.2-7.4 (Hayat, 2000). A mixture of formaldehyde and glutaraldehyde creates an effective fixative solution (Karnovsky, 1965): first, the formaldehyde component penetrates the tissue rapidly and helps avoid damage to the fine structure and then, a more slowly diffusing glutaraldehyde stabilises the tissue more thoroughly and more permanently.

Though aldehyde-based fixation is effective and primarily used in connectomics, it is not artefact-free. The most significant artefact is the loss of extracellular space (ECS) (Harreveld & Malhotra, 1967). The ECS fills the spaces external to cell membranes with an interstitial fluid that closely resembles the cerebrospinal fluid. Cragg (Cragg, 1980) suggested a solution to this problem by immersing the tissue in an unbuffered sucrose solution before fixing the tissue in buffered glutaraldehyde. Sucrose, a membrane-impermeant molecule, replaces the extracellular sodium and chloride and prevents the net inward ion flux, that leads to swelling in the only-aldehyde approach. Though the ECS does not con-

tain neural information, it aids the automatic analysis of neural circuits that uses machine learning algorithms (Pallotto et al., 2015). The authors in (Pallotto et al., 2015) have also proposed modifying the original Cragg's protocol to avoid excessive membrane shrinkage by regulating the osmolarity of the fixative buffer. The such adjustment also enables control of the ECS fraction in fixed tissue. Another benefit of the ECS preservation is that it allowed uniform staining of a 500 μm thick whole coronal cross-section slice of a mouse brain.

There are two major models of chemical fixation: (1) cardiovascular perfusion and (2) immersion fixation. Cardiovascular perfusion is believed to be the superior method for tissue preservation in most cases (Hayat, 2000). In this case, fixation begins immediately after the arrest of the systemic circulation, resulting in minimum alteration in cell structure. Furthermore, the fixative flow happens through the brain's extensive vascular system, increasing the penetration rate throughout the volume.

Staining with heavy metals

Osmium tetroxide (osmium, OsO_4) has been used since the early 19th century for the preservation of cellular detail of tissues for optical microscopy examination. It binds to most lipids and some proteins, enabling contrast staining of membranous structures, ribosomes, Golgi complex and mitochondria. With the emergence of electron microscopy, osmium, a heavy metal, was the first successfully used primary fixative for the ultrastructural preservation of animal tissues (Glauert, 1975). However, osmium has a slow penetration rate into most tissues and is unable to cross-link most proteins and preserve carbohydrates. Consequently, osmium is not used as a primary fixative for EM anymore but rather as a stain of the tissue already stabilised by aldehydes. Though osmium exhibits high electron density in EM, the contrast of osmium alone is not enough for SEM imaging.

The introduction of thiocarbohydrazide (TCH) as a bridging agent between two osmium steps improved the membrane contrast and prevented excess charging in SEM (Seligman et al., 1966). This method is now known as OTO: osmium - TCH - osmium. TCH works by binding itself to the osmium already affixed to the tissue from the first osmium step and allowing the deposition of additional osmium to the original osmium sites. Later, reduced osmium has been shown to add contrast to specimens and preserve filaments and membranes (McDonald, 1984). That method became known as rOTO: reduced osmium - TCH - osmium. Karnovsky (Karnovsky, 1971) was first to suggest the use of potassium ferrocyanide ($K_4Fe(CN)_6$) to reduce osmium tetroxide and to improve membrane contrast

of the tissue. The rOTO protocol is a basic protocol for brain tissue preservation in connectomics.

Osmium staining for SEM can be further enhanced with uranyl acetate (UA), a heavy metal commonly used in conventional TEM tissue preparation. Using uranyl acetate in combination with lead stains has an additive effect since UA acts as a mordant for the deposition of more stains (Dykstra & Reuss, 2003). Following rOTO with UA and lead aspartate stain produces the best high-contrast results for electron microscopy. The drawback is the small penetration depth of the staining, which has only recently become a concern with the growing need for large imaged volumes.

Method	rOTO	BROPA	ORTO
1$^{\text{st}}$ Os step	OsO_4 + $K_4Fe(CN)_6$	OsO_4 + $K_4Fe(CN)_6$ + formamide	OsO_4
			$K_4Fe(CN)_6$
additional Os step		OsO_4	
Amplification	TCH	Pyrogallol	TCH
2$^{\text{nd}}$ Os step	OsO_4	OsO_4	OsO_4
Enhancement	UA*		UA
	Lead Aspartate*		Lead Aspartate
penetration depth	< 0.2 mm	whole brain	0.5 mm

Table 2.1: Comparison of various staining methods. (* - optional)

Although the basic principles remained unchanged during the past decade, significant advances have occurred in methodology for EM preparation of tissue, especially of large volumes. The first protocol that helped overcome the limitation of osmium stain penetration and allowed for staining the whole mouse brain was BROPA protocol (Mikula & Denk, 2015). The protocol includes three main improvements to the original rOTO protocol. (1) The first osmium step is the reduced osmium dissolved in a formamide solution. Formamide helps penetration mainly because the tissue that is not yet robustly stained with heavy metals expands with this treatment, allowing for more space for the osmium to go through and therefore penetrate deeper into the tissue having fewer barriers. (2) An additional osmium tetroxide step is introduced before a mordant. (3) The protocol's main innovation is using pyrogallol as a bridge reagent instead of TCH. TCH produces extensive damage to the sample due to the liberation of N_2 during the reaction with the tissue. This

original whole-brain protocol was later adjusted to smaller samples, with an opportunity to enhance the contrast further with UA and Lead steps (Genoud et al., 2018).

Around the same time, another modification of the original rOTO protocol was published (Hua et al., 2015) (named ORTO in this work) that provides a homogeneous contrast in 1 mm^3 blocks of mouse brain tissue. The main modifications were: (1) splitting the reduced osmium step into two: first, impregnating the tissue with osmium tetroxide and then reducing it with ferrocyanide; (2) following the UA step, which usually takes place overnight at 4 °C, with 2 h at 50 °C.

Table 2.1 compares these protocols.

Dehydration, infiltration and embedding

For use in the GCIB-mSEM setup, tissue specimens must be sectioned into semi-thick sections. For sectioning, the specimen must be embedded in a suitable medium to provide stability to the brittle stained tissue.

The most suitable medium for EM is epoxide resins (Birbeck & Mercer, 1956; Glauert et al., 1956). Most epoxides are immiscible with water and will fail to polymerise properly if the tissue is not totally dehydrated. Because epoxy resins are soluble in ethanol, acetone and propylene oxide, dehydration is typically carried out with one of those solvents. Most protocols suggest a passage through acetone (Hua et al., 2015; Song et al., 2022) or propylene oxide (Mikula & Denk, 2015; Genoud et al., 2018) to make up diluted epoxide mixtures during the initial resin infiltration. These transitional solvents are better for the resins than straight ethanol, though propylene oxide is more toxic than acetone and has no features to recommend its use (Dykstra & Reuss, 2003).

There are various approaches to dehydration, some involving more incremental steps and some involving longer steps. Usually, three quick distilled water rinses after the last heavy metal step are followed by room or fridge temperature washes in 50%, 75%, 95%, two times in 100% ethanol, and finish with three longer washes with 100% acetone or propylene oxide before beginning epoxide resin infiltration steps (Hayat, 2000). Resins with higher viscosities, which epoxide resins are, benefit from longer infiltration times, more gradual steps involving diluted resins, and rotation or tumbling of the specimens during infiltration (Dykstra & Reuss, 2003).

The choice of moulds is determined by the characteristics of the embedding medium employed and the need for specific specimen orientation. Flat embedding moulds made of silicone rubber permit sample orientation.

Epoxy resin

Epoxy resins are a class of reactive polymers which contain epoxide groups - a triangular configuration of an oxygen atom bridging two carbons of an organic molecule. Epoxy resins require cross-linking agents, usually referred to as hardeners, such as polyfunctional amines, acids and acid anhydrides, phenols, alcohols and thiols (May, 1988), to convert them to tough and durable solids. The choice of a hardener depends on the application and handling characteristics, including viscosity and pot life (Sabu Thomas, 2014). Epoxies cured with anhydrides produce epoxy systems that exhibit excellent thermal, mechanical, and electrical properties (May, 1988), low shrinkage and remarkable stability under electron bombardment (Hayat, 2000), which makes them ideal for EM preparation. The only disadvantage is that the epoxy-anhydride combination requires heat for curing, and the curing reaction is slow even at $200\,°C$ (Fisch et al., 1956; Fisch & Hofmann, 1954). The addition of small quantities of accelerators, such as tertiary amines, carboxylic acids and alcohols, speeds up the curing process. Curing induces residual stress in epoxy systems (May, 1988), which is highly undesirable for a fragile biological sample. The use of flexibilisers helps alleviate this stress (May, 1988).

Embedding and sectioning qualities depend on the cross-linking of the block; generally, linear, shorter polymers containing a few cross-links are easier to section. Reducing the anhydride to epoxy ratio results in a shorter polymer with fewer cross-links, improving the embedding and sectioning quality (Hayat, 2000). A combination of nadic methyl anhydride (NMA) and dodecenylsuccinic anhydride (DDSA) gives good control over the hardness characteristics of the resulting block, which also defines the embedding and cutting qualities of the block (Burke & Geiselman, 1971). Epoxy resin sees an improvement in embedding and sectioning when the embedding medium contains 0.5-1.0% lecithin (Mollenhauer, 1986). However, lecithin is not readily soluble in resin, therefore, it is suggested first to dissolve it in peanut oil in a 1:1 ratio.

Spurr's resin

Spurr introduced ERL-4206 (vinyl cyclohexene dioxide) as an embedding medium for electron microscopy (Spurr, 1969), which has one of the lowest viscosities among all known resins used for this purpose. The low molecular weight, low viscosity and ability to stay fluid longer than other commonly used resins enhance its penetration into tissue. In addition to ERL-4206, The Spurr's resin consists of three more components: (1) nonenyl succinic anhydride (NSA) that acts as a hardener, (2) diglycidyl ether of polypropylene

glycol (DER 736) that serves as a flexibiliser, and (3) accelerator dimethylaminoethanol (DMAE). Both hardener and flexibiliser were chosen by Spurr due to their low viscosities. At the same time, DMAE was selected over benzyldimethylamine (BDMA) and tris(dimethylamino-methyl)phenol (DMP-30) for a longer pot life and, therefore, it can facilitate longer infiltration steps.

Over time, there have been many concerns regarding the toxicity and potential to cause cancer of the original ERL-4206 formulation. In 2005, ERL-4206 was taken off the market and replaced with ERL-4221 (epoxycyclohexylmethyl-3,4-epoxycyclohexylcarboxylate), a cyclic epoxide with greater molecular weight and viscosity. Despite the instruction from the vendors that ERL-4206 can be directly substituted with ERL-4221 as in (Spurr, 1969), the resulting blocks lacked the sectioning qualities of the original formulation (Ann Ellis, 2018).

Hard-Plus Resin-812

Hard-Plus Resin-812 is a newly formulated low-viscosity resin advertised as an improved Epon-812 — a high-viscosity resin. Epon-812 for electron microscopy consists of Epon 812 resin, DDSA and NMA anhydrides and DMP-30 accelerator (Burke & Geiselman, 1971). Besides this information, there is no public data about the composition of Hard-Plus Resin-812. This resin comes only as a premixed kit that contains Hard-Plus Resin-812, Hardener Hard-Plus and an accelerator.

2.2   Materials and Methods

Mice handling and section extraction

The mice handling procedure was approved by the local animal care committee and was in accordance with the laws of animal handling issued by the German federal government.

Transcardial perfusion

Mice were anesthetized through intraperitoneal injection of the mixture of ketamine and xylazine at the lower right quadra of the abdomen. The mouse reaching the surgical plane of anesthesia was assessed by loss of response to toe pinches. The mice were then transcardially perfused with cacodylate buffer followed by a fixative solution. The brain was dissected and post-fixed overnight at 4 °C in the fixative solution. Then, slices of of 500 μm were cut at 4 °C on a vibratome (VT1200 S, Leica Biosystems) in cacodylate buffer. Slices were then rinsed with cacodylate buffer five times over at least two days.

Immersion fixation

Mice were decapitated and the brain was then swiftly dissected, and slices of 500 μm were cut at 4 °C on a vibratome (VT1200 S, Leica Biosystems) in ACSF. Slices were then transferred into a fixative solution for an overnight fix at 4 °C and subsequently rinsed with cacodylate buffer five times over at least two days.

Artificial cerebrospinal fluid (ACSF)

124 mM NaCl, 3 mM KCl, 1.3 mM $MgSO_4 \cdot 7H_2O$, 84 mM $NaHCO_3$, 1.25 mM $NaH_2PO_4 \cdot H_2O$, 20 mM glucose, 2 mM $CaCl_2 \cdot 2H_2O$ are mixed with DD water and equilibrated with a 95% O2 – 5% CO_2 gas mixture. This solution is prepared fresh on the same day the brain slicing is performed.

Cacodylate buffer (CB)

A stock solution is prepared with 0.6 M sodium cacodylate in DD water, pHis adjusted with 0.6 M hydrogen chloride to 7.4. The stock solution can be prepared in advance and stored in the fridge. The working buffer is diluted with DD water or other chemicals to desired molarity.

Fixative

2% glutaraldehyde buffered with $0.2\,M$ cacodylate, prepared on the day the fixation is performed.

Pyrogallol

A stock solution is prepared by dissolving $1.28\,M$ pyrogallol in DD water. The stock solution can be prepared in advance and used up to 6 weeks after preparation. The working $320\,mM$ solution is then obtained by diluting the stock solution with DD water.

Uranyl acetate

The desired concentration of uranyl acetate is obtained either by mixing the uranyl acetate powder in DD water or by diluting the ready available aqueous solution with DD water. The solution obtained from the powder is filtered before use.

Walton's lead aspartate

Aspartic acid is mixed with DD water in the ratio of 0.4% w/v at $60\,°C$, then 0.66% w/v of lead nitrate is added to the mixture and let to stabilise. The pHis then adjusted at $60\,°C$ with $1\,M$ NaOH to 5.5. The solution is prepared on the day of the staining and is kept at $60\,°C$ throughout the staining process.

Hard-Plus Resin-812

The two resin components are mixed on the rotational mixer for at least $30\,min$, then the accelerator component is added, and the mixture keeps rotating on the mixer for another $30\,min$. The mixture is then either dissolved with acetone for partial infiltration steps or degassed for the final infiltration and embedding steps.

Spurr's resin

The three resin components are mixed on the rotational mixer for at least $30\,min$, then the accelerator component is added, and the mixture keeps rotating on the mixer for another $30\,min$. The mixture is then either dissolved with acetone for partial infiltration steps or degassed for the final infiltration and embedding steps.

Imaging in SEM

Surfaces were imaged using an In-Lens detector with primary electron landing electron energy of $1.5\,\mathrm{keV}$ and $1.6\,\mathrm{pA}$ current.

2.3   Results and Discussion

Before we started the preparation of the whole coronal cross-section slices of a mouse brain, we defined the volume parameters of the sample. There is a limit to the surface area because of the width of the knives (DHJ4580, DiATOME) we use and the travel range of the ultramiccrotome (Leica UC7, Leica Microsystems): 8 mm and 15 mm respectively. The existing staining protocols, apart from BROPA, are optimised for slices with a maximum thickness of 0.5 mm, therefore we adopted the same thickness for our samples. To evaluate the staining and imaging quality in SEM, we used the In-Lens detector in a single beam Zeiss Merlin EM, as this detector is similar to the detector used in Zeiss mSEM.

Initially, we followed the ORTO (Hua et al., 2015) protocol precisely, including cardio-vascular perfusion, all the staining modifications and the two-step infiltration with Spurr's. However, we found both staining and sectioning (Figure 2.2, left) unsatisfactory for GCIB-SEM purposes. The penetration of heavy metals was limited to 200 µm and the stained tissue had tears over its entire surface.

To address these issues, we then tried a different protocol, that included immersion fixation to preserve ECS and the rOTO staining approach with uranyl and lead enhancement Pallotto et al. (2015). The embedding steps were not described in that paper, therefore, we kept the same infiltration and embedding protocol as in (Hua et al., 2015). Additionally, we substituted Epon with Spurr's because Epon shows poor milling quality in GCIB (Hayworth et al., 2020). As a control, we tested all four permutations of fixation and staining. Neither of the samples yielded satisfactory cutting quality. However, both staining procedures that followed immersion fixation with ECS preservation showed heavy metal penetration throughout the whole sample and good contrast in the SEM (Figure 2.1). Therefore, we concluded that ECS preservation is important for stain penetration.

Additionally, we tested pyrogallol for amplification, as (Genoud et al., 2018) reported that in BROPA staining pyrogallol amplification shows better contrast than amplification with TCH. Specimens with higher contrast allow for faster imaging in SEM, which reduces overall processing time. This reduction is desirable for feasible large volume acquisitions. To denote the use of pyrogallol in a protocol, we use P instead of T in the protocol names: rOPO or ORPO.

To test the contrast of the stained tissue of each staining protocol, we collected a 90 nm section from each block on the same silicon wafer so all four can be imaged in the electron microscope under the same imaging conditions. The sensitivity of the detector was set such that the "no-signal" grey-scale level is 250 and the detector is not saturated. Figure 2.1

(top) shows *inverted* EM images — the contrast ranges from black at the highest intensity to white at the lowest — of sections stained with four different protocols. We assessed contrast visually and used histograms of the EM micrographs to quantify the contrast. Sections that have good contrast by visual inspection — rOTO and rOPO — also show three peaks in the histogram, while ORTO and ORPO — only two. The lowest intensity peak in all four histograms corresponds to the extracellular region filled with epoxy. The brain's extracellular matrix is composed of proteins and polysaccharides (Lam et al., 2019), that are only marginally affected by heavy metal staining. The two other modes in the histograms are that of the membranes and cytosol — the fluid inside the cell. The ORTO and ORPO protocols show a significant overlapping of these distributions, decreasing the membrane contrast. In the case of rOTO and rOPO protocols, the membranes and cytosol distributions are more spread out and their peaks, though largerly overlapping, can be easily separated: the membranes have a higher signal than the cytosol.
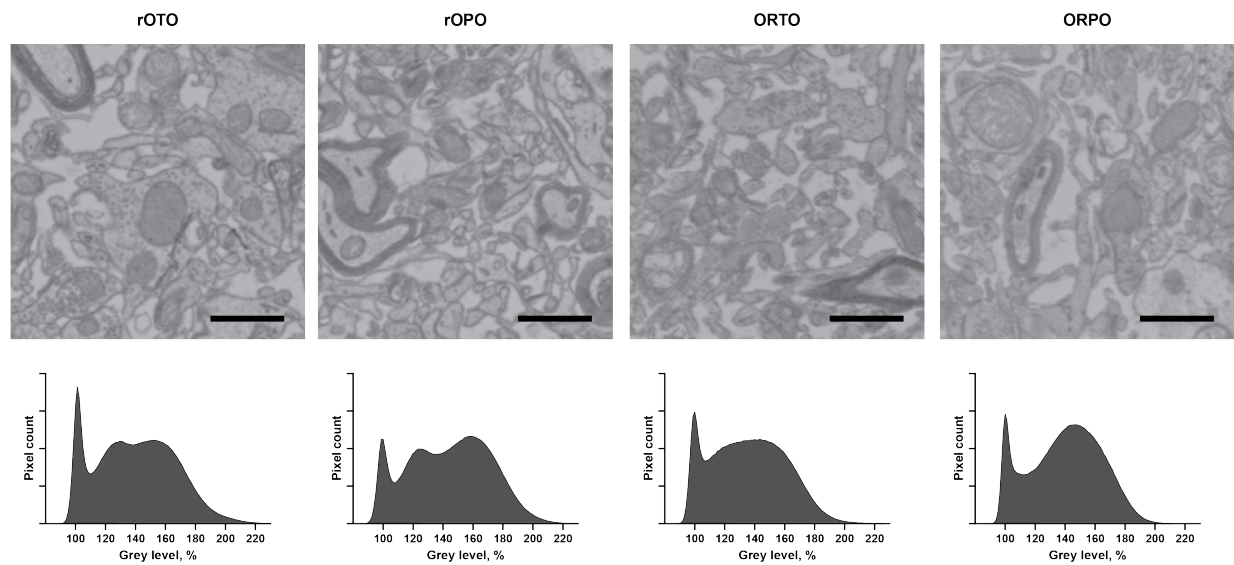

Figure 2.1: Top row: inverted EM In-lens images of 90 nm thick sections collected from 0.5 mm thick whole-coronal cross-sections stained with four different protocols: (a) rOTO, (b) rOPO, (c) ORTO, (d) ORPO. Bar is 1 μm. Bottom row: normalised histograms of the obtained images.

To quantify the contrast we flipped and re-scaled the histograms such that the "no-signal" grey-scale level referred to 0% and the ECS peak referred to 100% (Figure 2.1,

bottom). The contrast is then given by:

$$C = \frac{I_A - I_B}{I_A + I_B},\tag{2.1}$$

where I_A and I_B are the grey-level intensities of the peaks of tissue elements A and B. From this formula, we calculated the ECS-membrane contrast for all the used protocols and cytosol-membrane contrast for rOTO and rOPO protocols (Table 2.2). These calculations confirmed that pyrogallol indeed provides better contrast in SEM; and out of all four tested protocols we concluded that rOPO protocol has the best overall contrast. Therefore, the rOPO protocol is used in all the subsequent experiments.

	rOTO	rOPO	ORTO	ORPO
ECS-membrane	0.142	0.162	0.107	0.118
cytosol-membrane	0.066	0.100	NA	NA

Table 2.2: Calculated contrast of ECS and cytosol region in relation to the membranes for the four protocols.

Addressing the issue of poor sectioning, we tested whether the composition of epoxy plays a role in sectioning quality, since it was reported that Spurr's epoxy with the substituted ERL-4221 lacked the sectioning qualities of the original formulation (Ann Ellis, 2018). Because shorter polymers show better sectioning qualities (Hayat, 2000), we decreased the curing times from 48 h to 12 h — the shortest curing time that produced a fully polymerised block. Additionally, we tested the use of a combination of NMA and DDSA in ratios: 0.5:0.5, 0.65:0.35, 0.75:0.35, 0.80:0.20, 0.35:0.65, 0.25:0.75. Following the results of (Burke & Geiselman, 1971) which showed that a reduction in anhydride to epoxy ratio resulted in better cutting blocks, we gradually decrease the anhydride:epoxy ratio from 0.88:1.0 to 0.8:1.0, 0.75:1.0, 0.7:1.0, 0.65:1.0, 0.6:1.0 testing with each combinations of NMA:DDSA. Finally, all permutations we also tested with lecithin. Unfortunately, none of the modifications improved embedding quality.

Subsequently, we examined the possibility that the source of poor embedding quality was dehydration and/or infiltration. To ensure total dehydration of the samples, we used ethanol and acetone, which are highly hygroscopic, from freshly opened bottles. We also altered the infiltration process adding 25% and 75% resin steps and extending duration of each step to 48 h, except for the 100% resin step, at which resin was renewed twice with a fresh mixture over those 48 h. Making changes to dehydration and to infiltration lead to an

improvement in the cutting quality, but the improvement was not consistent. We achieved best sectioning quality when combining changes to both dehydration and infiltration.
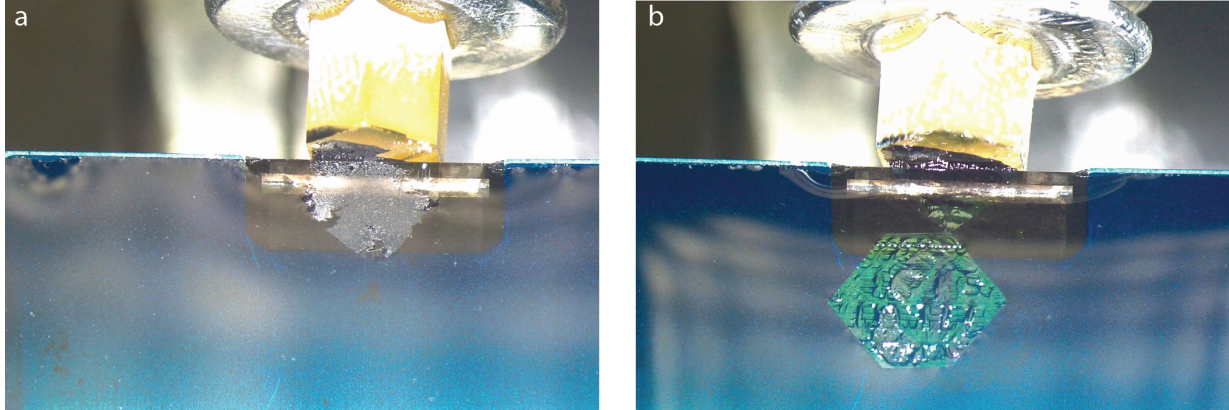

Figure 2.2: Examples of cutting (a) a poorly infiltrated sample and (b) a sample with good infiltration. (a) Section is falling apart and is grey in appearance due to the fact that the tissue is not held together by the epoxy. (b) Section with stained tissue that is held together by the epoxy after a cut.

Along with the dehydration and infiltration steps' changes, we considered Epon, Durcupan and Hard-Plus Resin-812 as an alternative to Spurr's resin. Epon and Durcupan were ultimately excluded due to poor milling quality (Hayworth et al., 2020) and high viscosity, respectively. Visually inspecting for compression artifacts, we concluded that Hard-Plus embedded samples had a superior relative to Spurr's cutting quality, showing less compression and, therefore, fewer artifacts when collected on a wafer. However, there were concerns about its suitability for GCIB milling and In-Lens imaging as not all resins are ideal for this technique (Hayworth et al., 2020). Experimental results showed that milling of Hard-Plus sections at lower angles produced smooth surfaces across all milling cycles chapter 5.

2.4   Summary

The result of this chapter is a protocol for 500 µm thick whole-coronal cross-sections enabling all further investigation in the following chapters. The complete protocol is outlined in Appendix B.

The research concluded the importance of ECS for stain penetration in large volumes and the significance of longer infiltration and dehydration steps in the preparation for sectioning. Immersion fixation produces satisfactory results at 500 µm but with even thicker sections, it might not be the best approach to preserve the tissue due to slow penetration of the aldehydes that can lead to damage in the core of the section. Therefore, if thicker specimens are necessary, one might consider optimising transcardial perfusion protocols for ECS preservation.

Analysing the micrographs of the stained sections, we found that better contrast corresponded with three recognisable peaks in the histograms. Using the degree of this separation as a measure of contrast, we observed that dividing the reduced osmium step into initial tissue impregnation and subsequent reduction as it is done in ORTO and ORPO protocols reduces membrane contrast. Furthermore, we confirmed that pyrogallol offers better contrast in the rOPO protocol, as was shown in experiments with BROPA.

Chapter 3

Sectioning and Positioning of the Samples

Entire biological specimens are too thick to be imaged with high precision in SEM due to the charge accumulation during imaging. Thus, the apparent need for sectioning. To obtain a high-quality electron micrograph of individual sections, they must be free from artefacts like charging, chatter, wrinkles, breaks and folds.

As soon as the sections are deposited on a silicon wafer, they are ready to be imaged. For efficient imaging in SEM, it is crucial to ensure that the slices are (1) conductive and (2) precisely located on the wafer. The next chapter investigates the first point, while the second is explored here. Described are methods of collecting consecutive sections on a wafer and creating the metadata for efficient imaging in the mSEM.

Specifically, this chapter provides a brief overview of cutting with a diamond knife and the role that various parameters play in the quality of the obtained sections. The goal is to collect sections on wafers and produce metadata files that include in wafer coordinates all section boundaries in addition to wafer to stage calibration data, allowing automatic movement of the microscope stage to selected points within each tissue section.

3.1 Introduction

At the outset, it is appropriate to clarify the terminology used in this thesis regarding the thickness of resin samples. The gradation of the thickness of the sections is the following: ultra-thin, semi-thin, thin and thick sections. Typically, ultra-thin sections are below 100 nm, semi-thin sections are between 100 nm and 2.5 µm, thin sections have a thickness of 2.5 µm - 20 µm and everything over 20 µm are thick sections.

Most advances in sectioning were made in preparation for TEM imaging, though only for very limited volumes of tissue, as only ultra-thin sections can be used in that type of microscopy. Though, with the invention of ATUM-tom(Hayworth et al., 2006), the approach of collecting ultra-thin sections was also adopted for SEM imaging(Tomassy et al., 2014; Kasthuri et al., 2015; Morgan et al., 2016; Hildebrand et al., 2017). With the introduction of FIB-SEM, the need for semi-thin and thin sections arose, and sectioning with a hot-knife was explored (Hayworth et al., 2015), which employed heating the cutting edge of the knife that locally heats and softens the block's surface, making it possible to cut sections thicker than 10 µm.

In this thesis, cutting is primarily done on an ultramicrotome (Leica UC7, Leica Microsystems), using a diamond knife (8mm, 45-degree angle) with a fixed cutting plane. While positioning the sample, the arm with the sample can be moved laterally; it only moves up and down during the cut. The advance of the sample arm after each cut determines the cutting thickness.

Cutting with a diamond knife

The factors that determine the quality of sections are the cutting medium, knife's material, clearance and bevel angles, the cutting speed, and the embedding material Hayat (2000). In addition, sectioning should be carried out in a room free of dust, draft, and vibration. Embedding material is one of the determining components that define sectioning quality. Epoxy resins co-polymerise with the stained tissue, reducing heterogeneity of the embedded block and resulting in smooth sectioning.

Cutting medium

As sections are cut, they float onto a liquid, which is in direct contact with the knife's cutting edge. The reasons for floating sections on a liquid are twofold: (1) surface tension forces of the liquid help restore the sections to their almost original dimensions after be-
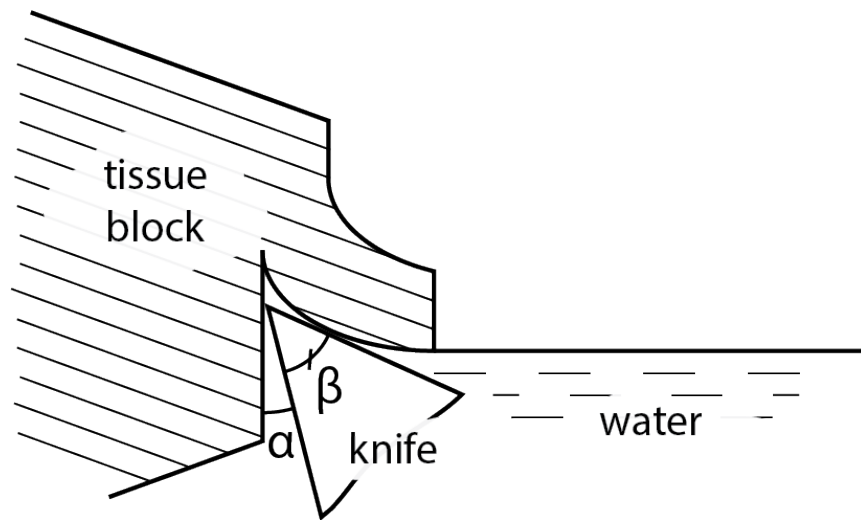
Figure 3.1: Schematic drawing of the sectioning process, indicating clearance α and bevel β angles.

ing compressed during cutting, and (2) liquids help transfer the sections to the imaging substrate. The desirable characteristics of the fluid are the following: (1) it should not damage cell ultra-structure, (2) it should easily wet the entire cutting edge of the knife, (3) it should absorb the heat generated as the lower surface of the section rubs the knife, (4) it should have a moderate surface tension, (5) it should not wet the sections. Distilled water is entirely satisfactory for sections of specimens embedded in epoxy resins.

With the introduction of a hot knife for thick sectioning, water was found to be ineffective, so the authors of (Hayworth et al., 2015) explored the possibility of oil for knife lubrication, which showed a dramatic improvement in surface quality.

The knife and its clearance and bevel angles

The knife edge needed for cutting thin sections must be sharp and hard. Diamond is the hardest known material, the most wear-resistant, and the best heat conductor of all known materials and is consequently used in sectioning for EM. Though even diamond knives, after an extended period of use, can become dull, introducing artefacts into the cutting process. In this case, the blade of the knife must be resharpened.

The clearance angle α is formed between the cutting edge of the knife and the specimen surface (Figure 3.1). This angle is necessary to avoid the block face scraping the back of the knife after the section is cut, hence avoiding marks on the block face surface. Though, the clearance angle should be kept as small as possible because a knife with a large clearance

angle tends to scrape the sections off the surface instead of cutting them, resulting in chatter. Also, too large a clearance angle introduces excessive stress on the knife cutting edge, decreasing the useful life of the knife.

A knife bevel angle β is measured between the two facets that form the cutting edge (Figure 3.1) and is critical for keeping the compression to a minimum. A diamond knife of an adequate width for whole mouse brain sectioning - 8 mm - is only currently available with the 45° bevel angle.

Cutting speed

The rate at which the specimen block moves past the knife during the cutting phase is designated the cutting speed, expressed in millimetres per second. The contact between the knife and the specimen causes the specimen to compress and the knife to vibrate. As a rule, sectioning should be performed at relatively slow speeds to minimise excessive compression, that can lead to wrinkles and fine chatter parallel to the knife edge (Hayat, 2000). Furthermore, sufficient time should elapse between the cutting of two consecutive sections allowing the knife vibrations to relax, otherwise, the vibrations will overlap, resulting in variations in section thickness.

Serial sectioning and section collection

The major challenge in preparing serial sections does not reside in the microtomy itself but with the transfer of sections onto the substrate compactly, without wrinkling, overlaps and loss. A number of methods are developed for collecting serial sections on a substrate. The simplest method is to guide the cut sections by an eyelash tool to a substrate and, simultaneously lower the water level (Couve, 1986). Alternatively, the substrate can be placed in the cutting boat under an angle. When the top of the section touches the top non-immersed part of the substrate, it adheres to it, and the substrate then can be slowly withdrawn from the water (Blumer et al., 2002). Instead of an eyelash tool, the sections can be directed to the substrate with a magnet if the resin is augmented with a magnetic resin (Templier, 2019). Sections can also be collected on a flexible tape (Hayworth et al., 2006). Like a conveyor belt, the tape is submerged in the cutting boat to collect the sections at the same speed the sections are cut.

Mapping the coordinates

Collecting sections on a substrate poses the challenge of targeted image acquisition across the whole area of the substrate. For that purpose, the authors of the ATUM-SEM approach, created a MATLAB-based semi-automatic microscope control software package named WaferMapper [1]. The strategy is first to map the dataset using low-resolution imaging to get an overview image of the wafer, then to map the overview image to the microscope's stage space and execute automatic acquisition of the high-resolution images in the SEM. This software, however, is not suitable for our designed mSEM-GCIB setup because it is optimised for single beam SEM control and we not only use an mSEM but have a number of additional custom features.

Edge detection

In computer vision, edge detection is a process that attempts to capture the significant properties of objects in the image, such as discontinuities in the photometrical characteristics of objects, and to localise those variations. It is challenging to design a general edge detection algorithm that performs well in many contexts. One that is commonly used is the Canny edge detection algorithm (Canny, 1986). It includes five steps: noise reduction, gradient calculation, non-maximum suppression, double threshold, and edge tracking. The goal is to detect edges that are "significant" while rejecting edges that are not.

To localise the edges, i.e. to localise the variation in the image's grey levels corresponding to discontinuities in the photometrical properties, edge detection algorithms use differentiation operators. However, image derivatives are sensitive to various noise sources. Therefore, a smoothing operation is used first to reduce the noise and regularise the differentiation, leading to a trade-off between noise reduction and information loss. In the case of the Canny edge detector, noise reduction is performed by convolving a Gaussian filter with a kernel size $(2k + 1) \times (2k + 1)$ with the original image:

$$ K_{i,j} = \frac{1}{2\pi\sigma^2} exp\left(-\frac{(i-(k+1))^2 + (j-(k+1))^2}{2\sigma^2}\right); 1 \leq i,j \leq (2k+1). \qquad (3.1) $$

This filter is invariant to rotation, ensuring a smoothing effect irrespective of edge orientation.

---

[1] https://wafermapper.googlecode.com

For differentiation, the Canny edge detection algorithm uses a gradient derivative operator — detecting the edge intensity and direction by calculating the gradient of the image. The operators use two 3×3 kernels G_x and G_y, which are convolved with the original image to calculate approximations of the derivatives in both directions: horizontal (x) and vertical (y):

$$G_x = \begin{pmatrix} -1 & 0 & 1 \\ -2 & 0 & 2 \\ -1 & 0 & 1 \end{pmatrix}, G_y = \begin{pmatrix} 1 & 2 & 1 \\ 0 & 0 & 0 \\ -1 & -2 & -1 \end{pmatrix}. \tag{3.2}$$

Convolution results in derivatives I_x and I_y. Then, the magnitude I and the slope θ of the gradient are calculated as follows:

$$I = \sqrt{I_x^2 + I_y^2}, \tag{3.3}$$

$$\theta = \arctan \frac{I_y}{I_x}. \tag{3.4}$$

To suppress thick edges and instead only return thin edges — the so-called non-max suppression step — the algorithm scans the points in the gradient intensity matrix and finds the local maximum values along each edge gradient. The resulting edge image has thinner edges but can still show variations in the intensity values each detected edges.

This shortcoming is rectified with the two final steps — double thresholding and edge tracking. In the double thresholding step, pixels are assigned one of three labels: strong, weak, and non-relevant. Strong pixels have an intensity so high that it is certain they constitute an edge, while non-relevant are those pixels with signal small enough to be considered irrelevant for edge detection. Finally, pixels between the two extremes are considered weak. The tracking edge step assigns weak pixels to the strong category when at least one of the surrounding pixels has the strong label. Otherwise, it placed in the non-relevant category.

3.2   Materials and Methods

Wafer preparation

For the experiments, 2-inch wafers with one flat were used (J12006, Siegert Wafer). The wafer's thickness is $(279 \pm 25)\,\mu m$, and the conductivity is $< 0.005\,\Omega\,cm$.

Plasma cleaning of the wafer

The wafers are placed in plasma cleaner (Plasma Cleaner PDC-32G, Harrick Plasma) and treated with air plasma for one minute.

Chemical clean of the wafer

Conversely, the chemical clean — the RCA-2 (Radio Corporation of America) — is done by soaking wafers in a cleanser solution for 10 minutes. The general recipe for RCA-2 cleanser is 6 parts water (H_2O), 1 part 27% hydrogen chloride (HCl), and 1 part 30% hydrogen peroxide (H_2O_2). The solution is mixed in a Pyrex beaker; when hydrogen peroxide is added, the solution will bubble vigorously for a few minutes. Silicon wafers, when finished, rinsed with clean DD water. RCA-2 clean should be performed in a laminar flow hood.

Diamond knife

Diamond knives of $8\,mm$ and $45°$ bevel angle (DH4580, DiATOME) were used for cutting the sections.

Optical image

Optical images of wafers were taken with a camera (Sony Alpha 7RII, Sony) and an objective macro lens (FE 90MM F/2.8G Macro OSS , Sony). The image is taken in complete darkness with an aperture f/2.8, $30\,s$ exposure, ISO-50 sensitivity, and flashlight at $\frac{1}{16}\,s$.

3.3   Results and Discussion

An untreated hydrophobic silicon wafer surface may cause wrinkles in the tissue due to the large water contact angle (Figure 3.2 top row) (Kubota et al., 2018). The water contact angle is 48° before the treatment, and after plasma or chemical treatment, silicon wafers show a shallower water contact angle, almost complete wetting, promoting smooth deposition of thin sections on the wafer.
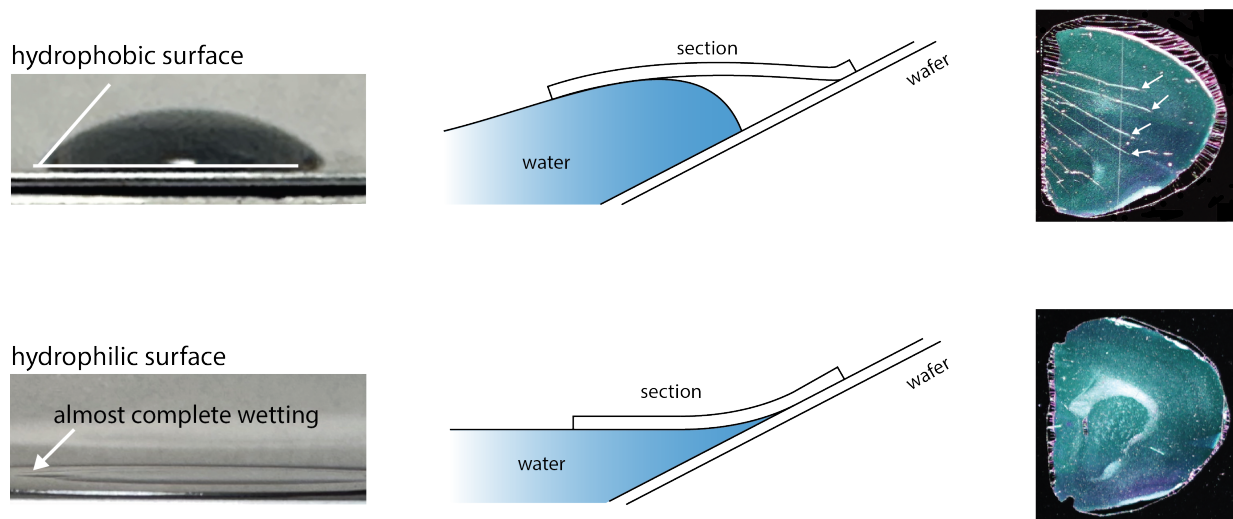

Figure 3.2: Comparison of (top) hydrophobic and (bottom) hydrophilic substrates. A water drop on an untreated silicon surface (top left) creates a large — 48° — water contact angle. Conversely, when dropped on to a treated silicon surface (bottom left) it almost completely wets it. When (top centre) there is a large water contact angle the section has no support at the deposition site, while (bottom centre) in the case of almost complete wetting the section is supported by the water at the deposition site. Optical image of the result of the deposition of 500 nm thick sections: (top) on to the hydrophobic surface which caused wrinkles (shown by the white arrows), (bottom) on to the hydrophilic surface upon which the section lay flat.

In the case of a hydrophilic substrate surfaces, the water and it's surface tension provide more support for the section as it is stretched out and deposited on the substrate. In the case of a hydrophobic surface, there is a larger angle between the section and the surface and part of the section has no support, resulting in wrinkles during deposition.

Wrinkles in the tissue cause information within the folded region to be missed during image acquisition. Consequently, it was important to treat the surface of each wafer before collection, in order to ensure the smooth deposition of the tissue.

Sectioning and collection

A standard and simple method to collect sections is to cut sections and then, using an eyelash tool, direct them towards the cleaned wafer. When the tip of the section reaches the wafer, it adheres to it. Then, slowly withdrawing the wafer from the water, the water is pulled from under the section, and the whole section adheres to the wafer.

Though this method works for relatively small areas ($<1\,\mathrm{mm}^2$), as the size grows, compression of the sections during cutting also increases to the point that the water surface forces are not enough to restore the sections to their original size. However, further relaxation can be achieved by heating the water and so we attached a heater and thermal control to the boat to provide consistent heating. In the case of the whole coronal cross-section of a mouse brain, 60 °C was deemed sufficient. The resulting surface of each section does not possess uniform thickness. As all embedded tissues are non-homogeneous, intra-section variation in thickness or surface roughness is common. A major reason for such variation is compression. A section undergoes an uneven thickening in the form of compression during cutting with a knife. Although the sections, when flattened with heat, revert towards their original shape, the recovery varies across the different parts of each section. This explains the difference in colour within and between the sections (Figure 3.6 right).

The significant difference in the degree of recovery between the epoxy embedded stained tissue and the surrounding blank epoxy, causes wrinkling of the blank epoxy when deposited as it relaxes more than the contained tissue (Figure 3.2 right). This is a problem, because the blank epoxy wrinkles not only charge in the mSEM degrading imaging, but can also cause wrinkles in the tissue. Therefore, we recommend trimming the tissue block as much as possible to preserve the necessary volume while removing blank epoxy around it.

Heating the water also means heating the whole boat and the knife. While they are heated, the knife fluctuates from its original position, causing non-uniform sectioning thickness. Therefore, these two processes must be separated either timely or locationally.

To achieve time separation, we first cut the necessary sections and then collect sections after they were relaxed with heat. To this end, one of the Leica microtomes was upgraded to hold a motorised linear stage (KMTS50E/M, Thorlabs) with a wafer holder (78410-2WFC, Electron Microscopy Sciences) Figure 3.3. We also designed a new knife boat to accommodate a 2-inch wafer, to which we attached heating elements (CSH-1011001/120V, Omega) and a temperature sensor PT-100. Unfortunately, this design limits the number of sections that can be collected in one cycle (Figure 3.6) and imposes the challenge of re-approaching the knife and long waiting times between heating and cooling the system.
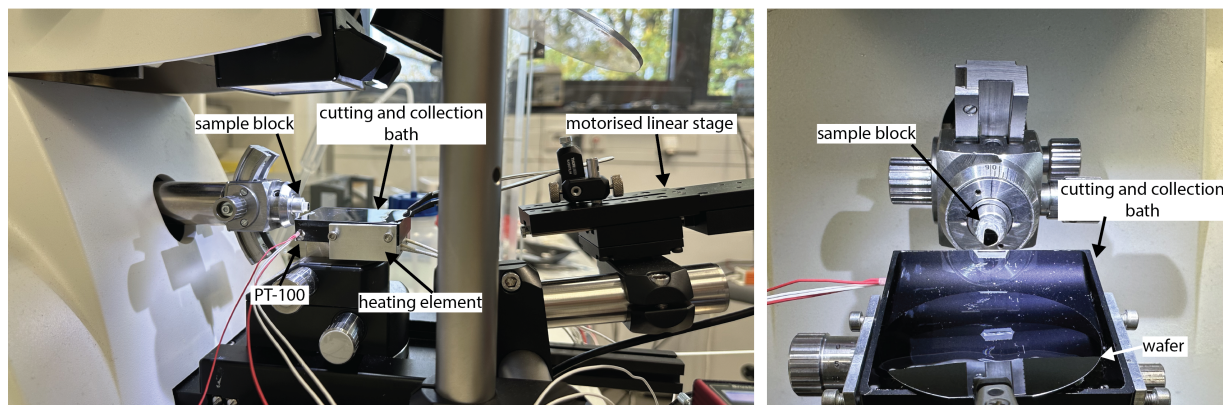
Figure 3.3: Section collection setup with time separation. On the left is the side view of the system. On the right is the front view of the cutting and collection bath.

To avoid these challenges, we separated sectioning and collection into different baths, i.e. locationally (Figure 3.4 a). To accomplish such separation, we manufactured a collection boat that also accommodates metal plates with heaters and a platinum resistance thermometer (PT-100). At the collection bath end, we installed two linear stages (VT-80, Physik Instrumente) creating an x-y stage that holds a wafer-holder with a wafer. In addition, we modified a standard knife bath (DH4580, DiATOME) to allow for the creation of a channel to the collection bath. We connected the two baths with a bellows to isolate the microtome from any vibrations created by the movement of the x-y stage, water-sealed the connection on either side and ran a Teflon tube through. The transfer between the baths occurs due to the over-pressure generated in the cutting chamber. The positioning on the wafer is still done manually with an eye-lash tool to ensure dense deposition on the wafer. We used this setup to fill a single wafer with consecutive sections (Figure 3.6 bottom row).

Unfortunately, this method is still limited in the amount of sections that can be collected. Even though there are no issues with the transfer of sections initially, after a while, sections begin sticking to the Teflon tube. This is likely a result of a local change of water meniscus from concave to convex inside the tube as the water is re-added after partial evaporation (Figure 3.5). At the start of section collection, we ensure that the meniscus inside of the tube is concave. This means that the potential energy of the section is minimised in the centre of the tube and it can travel through the channel without contact with the wall. If the trapped air does not allow for complete wetting after the re-adding of water, however, the position of minimised potential energy is changed and the section is pulled directly against the tube wall inhibiting its movement. To return the meniscus
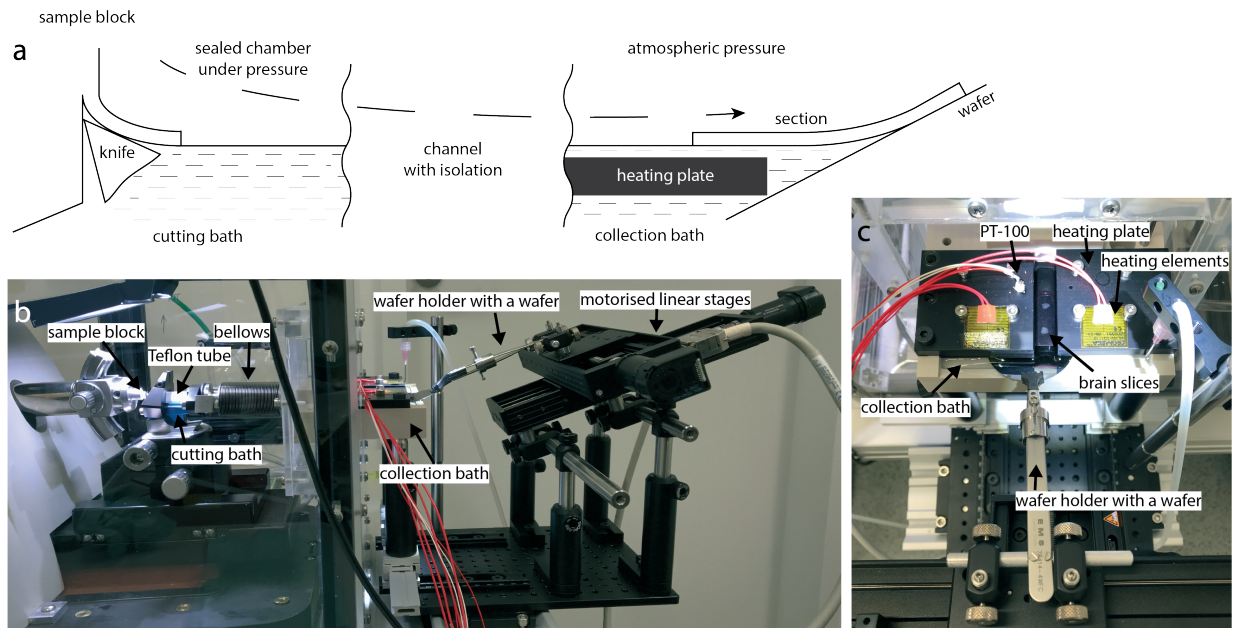
Figure 3.4: Section collection setup with location separation: (top) schematic, (bottom left) a view from the side, (bottom right) a view from the front of the collection bath.

to its concave state requires partial disassembly of the system to clean the tube walls and, therefore, change of the alignment and position of the knife. Re-approachment of the knife to the sample may lead to the loss of some sections.
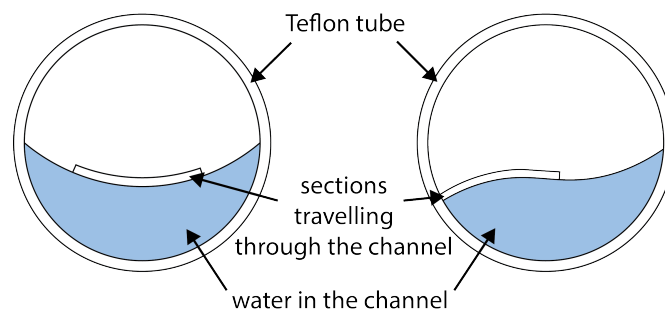

Figure 3.5: Cross-section of the Teflon tube channel during section transfer. The left side shows the ideal configuration where the section moves along a concave meniscus. On the right is a possible configuration of a convex meniscus.

We also attempted to automate the positioning of sections via directed air flow. The exact effect of the air flow strongly depends on the geometry and orientation of the sections making it quite challenging to determine the exact requirements to direct sections along

the entirety of the long path they must travel. This idea wasn't deemed feasible at this point in time, as it required constant supervision.

Optical image of the wafer

It is important to accurately locate sections avoiding empty space on the wafer for efficient imaging with the mSEM. The geometry of the imaging substrate and its position in the mSEM does not change from experiment to experiment; therefore, it is easy to establish an automated routine to pull information about regions of interest.

For this purpose, we take an optical image of the wafer with a camera (Sony Alpha 7RII, Sony) and an objective macro lens (FE 90MM F/2.8G Macro OSS , Sony). The system (Figure 3.6 left) also consists of a specially designed holder for the wafer and a camera flash. All of these parts sit on top of a rail (X90, Thorlabs) for easy adjustment when needed and securely fixed. The image is taken in complete darkness with an aperture f/2.8, 30 s exposure, ISO-50 sensitivity, and flashlight at $\frac{1}{16}$ s.
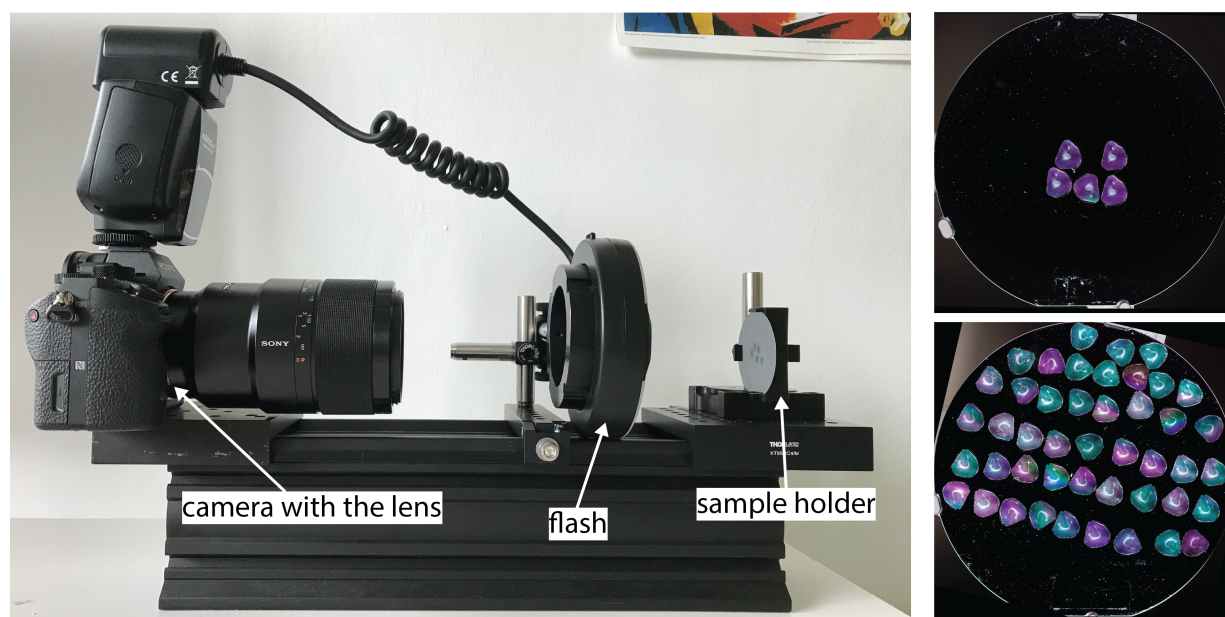

Figure 3.6: Camera setup for taking optical images of wafers (left) and examples of images (right)

The mSEM stage coordinates relative to the wafer are shown in Figure 3.7b. To unambiguously translate the coordinates from the obtained optical image to the stage coordinates, we chose a standard rotation for the optical image. Specifically, the image is

normalised when the wafer's flat is parallel to the x-axis as depicted in Figure 3.7a and the image is cropped to the diameter of the wafer.

We automated this normalisation process with a python script. First the circular edge of the wafer is detected using the `HoughCircles()` method from the `opencv` package in python. This method returns the centre and radius of the wafer in pixels. Next, the flat's location is found using the `HoughLinesP()` method from the same package. This method detects straight lines on the image and returns the extremes of the detected lines - information enough to calculate the angle of the flat in the not yet processed image. Knowing the angle, the centre and the radius of the wafer, rotation and cropping are done with `rotate()` and `crop()` methods from the `pillow` package in python. The resulting image is then saved as a normalised image (Figure 3.6 right), and the wafer's radius in pixels is written into a corresponding metadata file.
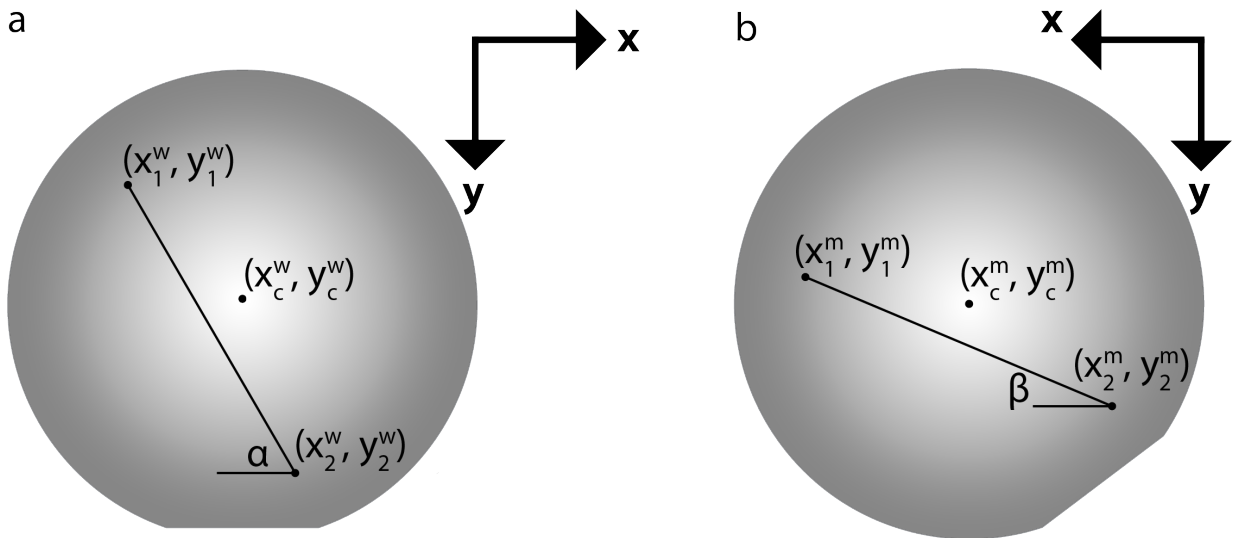

Figure 3.7: (a) Wafer coordinates. (b) mSEM coordinates

Knowing the wafer's radius in pixels, it is now easy to find the pixel-to-millimetre conversion ratio and define the *wafer coordinate system* (Figure 3.7b) in millimetres. The centre of the wafer coordinate system coincides with the centre of the normalised optical image. With the setup we have, the radius of the 2 inch wafer ($R = 25.4\,\text{mm}$) is around 2600 pixels, giving an optical image resolution of around $10\,\mu\text{m}$ per pixel. The imaging parameters in the mSEM are such that each of the 91 beams have a resolution of 1560×1360 pixels with each pixel being $10\,\text{nm}$ in size. Altogether, the 91 beams create a hexagon

with a diameter of 11 beams, producing an image with diameter of around 171 µm, which corresponds to 17 pixels in the optical image.

Usable wafer area

For efficient imaging, it is important to ensure that scanning happens over the regions with valuable information — i.e. over the tissue regions, and that the obtained image is not distorted. We observed, that at the edges of the wafer the mSEM beams are deflected, effectively limiting the usable area of the wafer. Consequently, we needed to ensure that we deposit the sections within this region during collection.
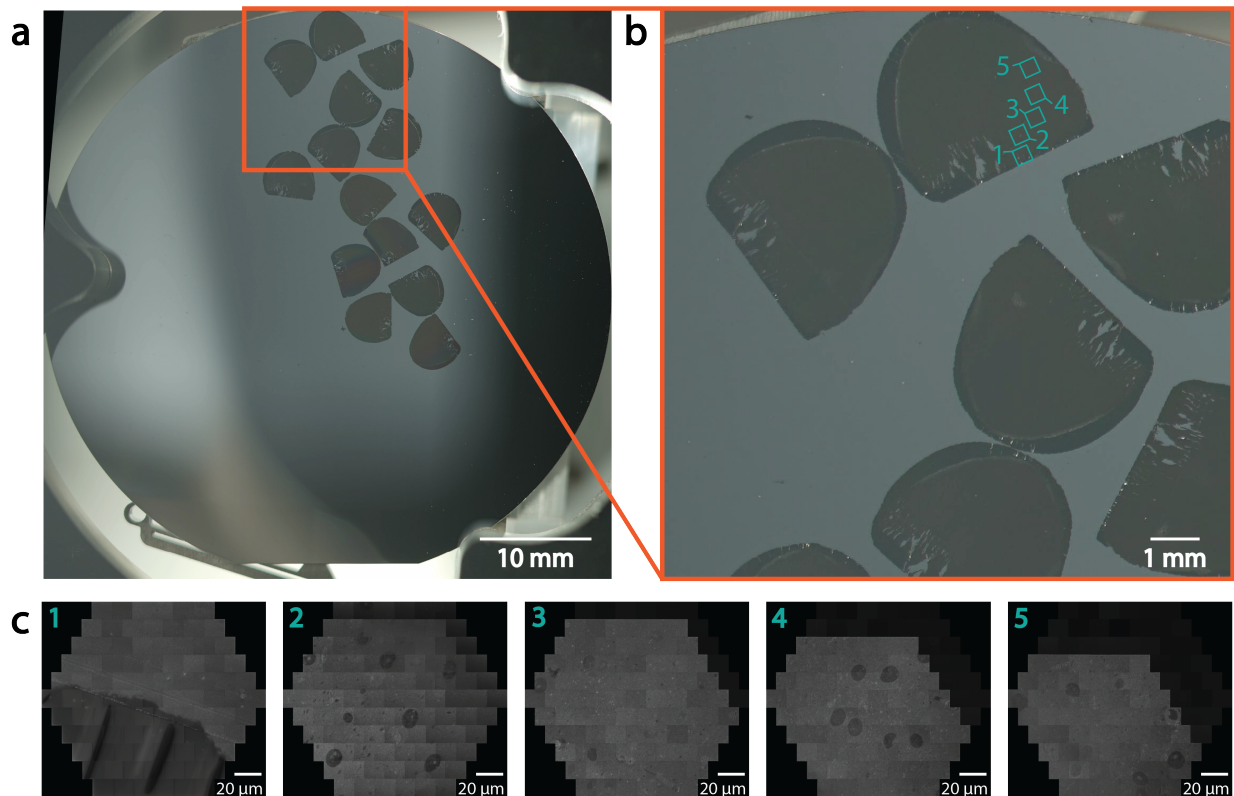

Figure 3.8: Imaging of the edge of the wafer in the mSEM. (b) A close-up of the (a) normalised light image of the wafer. (c) Imaged region corresponding to the boxes of (a). Distances from the centre/from the edge are 1) 22.39 mm/ 3.01 mm, 2) 22.94 mm/ 2.46 mm, 3) 23.16 mm/ 2.24 mm, 4) 23.61 mm/ 1.79 mm, 5) 23.94 mm/ 1.46 mm.

To determine the possible area where sections can be deposited, we placed tissue slices close to the wafer edge (Figure 3.8a) and imaged them in the mSEM. By navigating

the mSEM stage closer with each step to the edge, we noted the coordinates when the beams started to deflect (Figure 3.8) and then converted them into wafer coordinates. At 3 mm from the edge the mSEM hexagon is still fully detected, but starting at 2.5 mm the beams began to progressively deflect which is evident in the missing shells of the hexagon (Figure 3.8 c). From this calculation, we determined the usable area to be within a 22 mm radius from the centre of the wafer.

Transformation from wafer coordinates to multiSEM stage coordinates

To obtain coordinates in the *mSEM stage coordinate system* (Figure 3.7a), we have to flip about the y-axis (M_x), rotate ($R(\theta)$) and translate ($\vec{v}_T$) the wafer coordinates:

$$\vec{v}_N^m = R(\theta)M_x\vec{v}_N^w + \vec{v}_T \tag{3.5}$$

Re-insertion of even the same wafer into the mSEM stage might affect the rotation operator $R(\theta)$ and translation vector $\vec{v}_T$; therefore, calibration is recommended before each round of imaging.

Calibration starts by finding two predefined, spatially separated points with features easily identifiable in both optical and EM images. We find the points $(x_1^w, y_1^w), (x_2^w, y_2^w)$ in the wafer coordinates within the optical image with the help of the pixel-to-millimetre conversion ratio, while the mSEM stage coordinates $(x_1^m, y_1^m), (x_2^m, y_2^m)$ are known after finding the position of the points in the microscope.

We then calculate the rotation angle θ as follows:

$$\theta = \alpha - \beta = \arctan\frac{y_2^w - y_1^w}{x_2^w - x_1^w} - \arctan\frac{y_2^m - y_1^m}{x_1^m - x_2^m}. \tag{3.6}$$

Therefore, Equation 3.5 takes the following form:

$$\vec{v}_N^m = \begin{pmatrix} \cos\theta & -\sin\theta \\ \sin\theta & \cos\theta \end{pmatrix} \begin{pmatrix} -1 & 0 \\ 0 & 1 \end{pmatrix} \vec{v}_N^w + \vec{v}_T \tag{3.7}$$

The translation vector can be determined by finding the vector from either of the points to the centre of the wafer resulting in:

$$\vec{v}_T = \vec{v}_i^m - RM_x\vec{v}_i^w = \begin{pmatrix} x_i^m \\ y_i^m \end{pmatrix} - \begin{pmatrix} \cos\theta & -\sin\theta \\ \sin\theta & \cos\theta \end{pmatrix} \begin{pmatrix} -1 & 0 \\ 0 & 1 \end{pmatrix} \begin{pmatrix} x_i^w \\ y_i^w \end{pmatrix}, i = 1, 2. \tag{3.8}$$

Finally, we convert a point N in wafer coordinates to the mSEM stage coordinates as follows:

$$\vec{v}_N^m = \begin{pmatrix} \cos\theta & -\sin\theta \\ \sin\theta & \cos\theta \end{pmatrix} \begin{pmatrix} -1 & 0 \\ 0 & 1 \end{pmatrix} \vec{v}_N^w -$$

$$\begin{pmatrix} x_i^m \\ y_i^m \end{pmatrix} + \begin{pmatrix} \cos\theta & -\sin\theta \\ \sin\theta & \cos\theta \end{pmatrix} \begin{pmatrix} -1 & 0 \\ 0 & 1 \end{pmatrix} \begin{pmatrix} x_i^w \\ y_i^w \end{pmatrix}, i = 1, 2 \tag{3.9}$$

After the calibration is complete, the conversion from the pixel space of the optical image to the physical mSEM stage coordinates can be done automatically. We use this information to select the region of interest to be scanned by defining the regions' boundaries or to move the mSEM stage to a selected point on the image. In both cases, we implemented this functionality as a part of the GCIB-mSEM software as toggleable tools within the `matplotlib.pyplot` interface. Movement of the mSEM stage is initiated with Zeiss mSEM API by passing the converted coordinates into the move function.

Tissue boundaries

At first, we implemented the tissue boundary functionality as a toggleable tool within the `matplotlib.pyplot` interface that allows manual selection of a number of points around the tissue. Once defined, the functionality assigns an index number to the region and saves the selected locations in wafer coordinates in a metadata file associated with the wafer number.

With only a few sections, manual selection of tissue boundaries may be sufficient. However, as the number of sections grows, it is more beneficial to use an automated detection tool. Taking advantage of the different optical properties of the wafer and sections in the optical images (Figure 3.6 right), we decided to automate this process.

We started by applying the commonly used Canny edge detection method. For this we used `canny` method from `scikit-image` Python package with a Gaussian filter of various kernel sizes (Figure 3.9, top row), which resulted predominantly in detection of the wafer's edge as well as debris on the wafer, completely ignoring the tissue edges. To rectify the problem, we reasoned that (1) the contrast of the slices needed to be enhanced and (2) the accents around the edges of the wafer must removed.
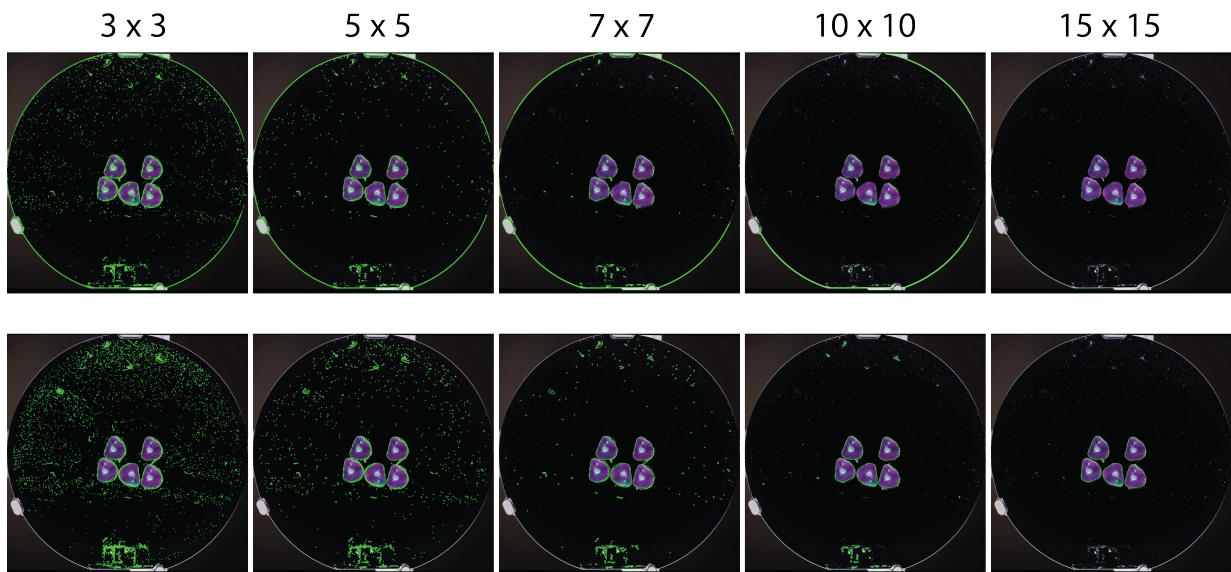
Figure 3.9: Contours (green) detected with the Canny edge detector with different Gaussian blur sizes (columns). The top line is the standard Canny edge detector applied to the original image. The second line is applied to the image after thresholding the original image at a 25 grey scale level and masking to include only 3 mm from the wafer's edge
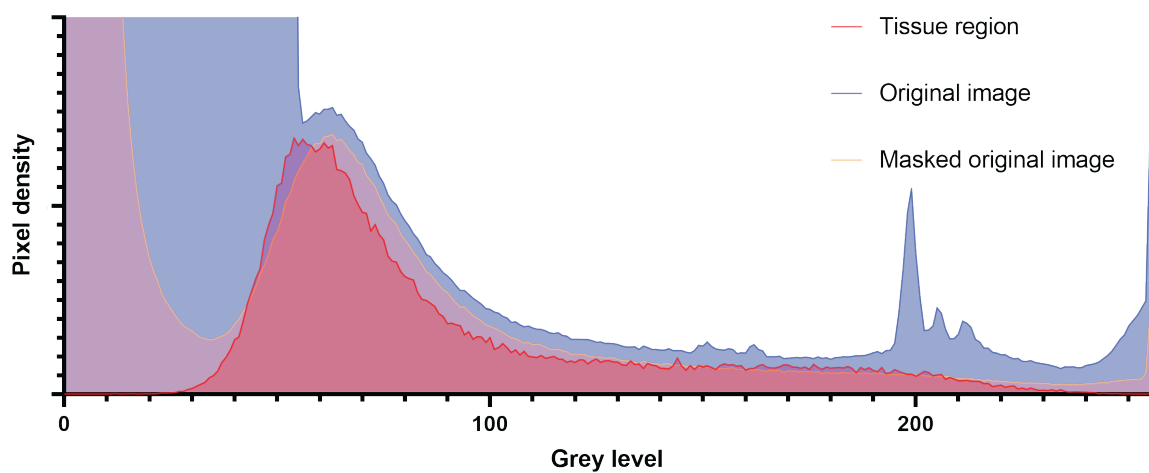

Figure 3.10: Histograms of grey-scale values in wafer images

To enhance the detection of the tissue we created a histogram and compared the distribution of grey-scale values of manually marked tissue with the values of the entire image (Figure 3.10). As seen in the figure, the grey-scale distribution for the wafer starts at 25 grey-scale units, however, there is a significant overlap of the background values with those of the tissue. Including only the usable region of the wafer (within a 22 mm radius) allows for a distinct separation between the sections and the background. Keeping this in mind, we introduced two steps before edge detection: (1) values of all the pixels above the 25 grey-scale units are set to 255 applying `threshold` method from the `opencv` python package and (2) all the pixels outside of the effective region are set to 0.

We then applied the same Canny edge detection method to the modified image (Figure 3.9, bottom row). With a kernel size of 15, the algorithm resulted in the almost exclusive detection of the edges of the sections. Though, the detected sections also included the epoxy. Blank epoxy does not contain information about the tissue, so it is not necessary to image it and the detection can be further optimised to just the tissue itself. This, however, is not going to be a problem if the epoxy was trimmed prior to deposition and the sections only contain tissue regions.
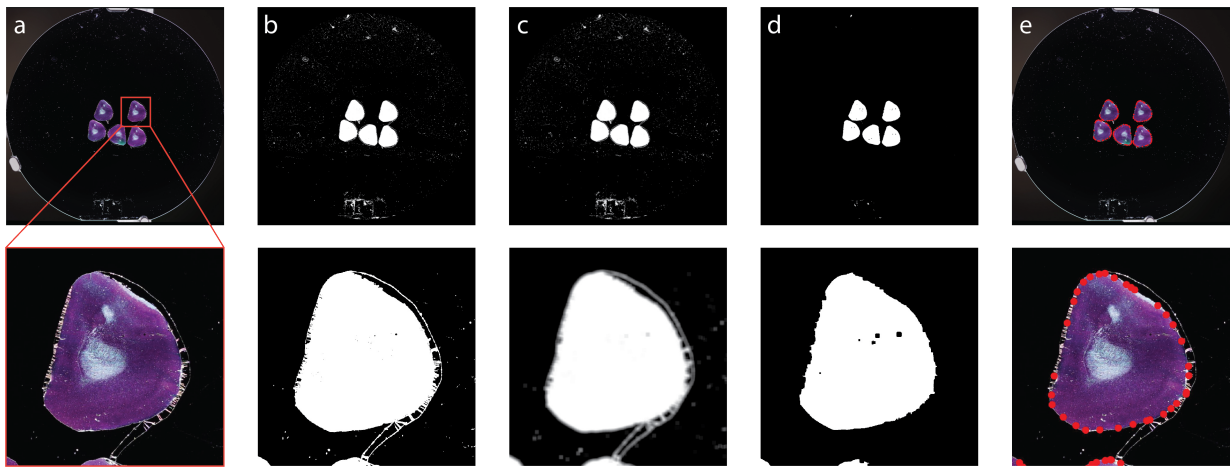

Figure 3.11: Steps of edge detection. (a) the normalised image, (b) a thresholded binary image, (c) with Gaussian blur, (d) the previous image with the second thresholding, (e) boundary points creating a convex hull.

Figure 3.11 (c) shows the image after Gaussian blur 15 that precedes the detection of the edges in the Canny algorithm. At this stage, the thin edges of epoxy have a lower grey-scale value, which means it possible to get rid of them by simply thresholding the resulting picture again. Figure 3.11 (d) shows the resulting image, on which only the tissue regions

have an intensity level of 255. At this point, the elaborate Canny edge detector is not really necessary and we detected the contours using `findContours` from the `opencv` Python package filtering the contours by their area. We then created a convex hull around each area, using the `convexHull` method of the same package. The resulting set of points (Figure 3.11e) surrounds the tissue and defines the tissue boundary. This boundary, as in the manual case, is assigned a wafer number and its coordinates are saved in a metadata file. In both cases, this information is used to find focus points within the tissue and to define regions for targeted imaging and milling.

We tested this algorithm on multiple wafers, including a wafer containing 45 sections, all of which were successfully detected with the algorithm Figure 3.12. Furthermore, we implemented it within the GCIB-mSEM software.
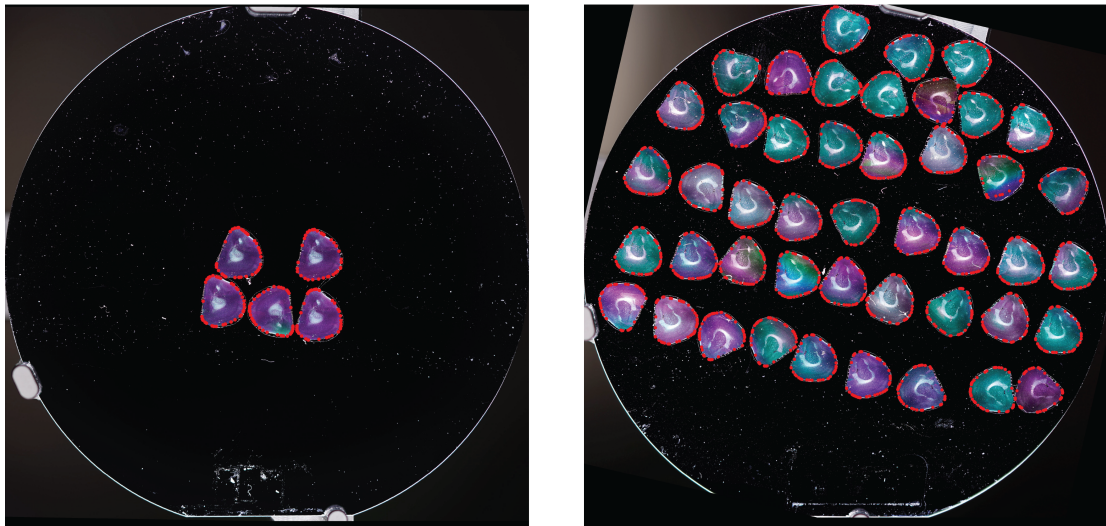

Figure 3.12: Results of the boundary detection algorithm

3.4   Summary

The silicon wafers need to be treated to make them hydrophilic, thereby ensuring the adherence of the sections to the wafer while maintaining a smooth tissue surface. Larger sections further necessitate heating to maintain tissue smoothness. Ideally, all excess embedding medium around the tissue block should be removed. This trimming will result in a block face of uniform density without wrinkles and will simplify the detection of tissue boundaries.

In order to ease navigation while imaging with the mSEM we make use of an optical image. After a calibration process, this image enables collection of coordinates to be imaged in the mSEM decreasing preparation time required for acquisition and removing any need for manual labor. These features exist within our GCIB-mSEM control software.

Chapter 4

Inducing Conductivity of Sections

Typically, a sample embedded in an epoxy resin is non-conductive. This means that during an electron beam scan, a sample will build up a static surface charge. When the accumulated surface charge reaches values as high as the electron beam acceleration voltage, the beam will reflect, not even reaching the surface. Subsequently, the detected signal would not provide information about the sample.

This chapter describes the ways of inducing conductivity in the samples and lays out the design of the system for inducing conductivity of samples for the GCIB-mSEM imaging.

4.1 Introduction

When the primary electron hits the sample, there are four possible outcomes: (1) it back-scatters and leaves the sample, (2) it causes an emission of secondary electrons, or (3) it is absorbed by the sample and (4) can leave the sample through grounding. The electron beam in SEM delivers a high number of electrons per second, so all three of these processes co-occur (Figure 4.1). The relative balance of each of the four possibilities determines the net charge of the sample's surface:

$$Q' = I_{PE} - I_{BSE} - I_{SE} - I_{GND}, \tag{4.1}$$

where Q' is the net charge accumulated on the sample over time, I_{PE} is the primary electron beam current, I_{BSE} and I_{SE} are the currents of back-scattered and secondary electrons respectively, and I_{GND} is the current passing through the sample to the ground.

For an electrically grounded sample, its conductivity defines the magnitude of I_{GND}: the higher the conductivity, the higher the current to ground. In the case of conducting samples, any excess electrons can easily pass through to ground, so the net charge Q' is virtually zero. Poorly conducting samples, however, will accumulate charge yielding a surface potential across the scanned region. This effect can be modelled in a simplified form as a parallel circuit consisting of a resistor and capacitor Figure 4.1.

The electric field produced by the surface potential decelerates the primary electron beam and accelerates the secondary and back-scattered electrons in a non-uniform way, distorting the image. When the surface potential reaches a value as high as the primary electron acceleration voltage, the incoming primary electrons are repulsed, not even reaching the sample.
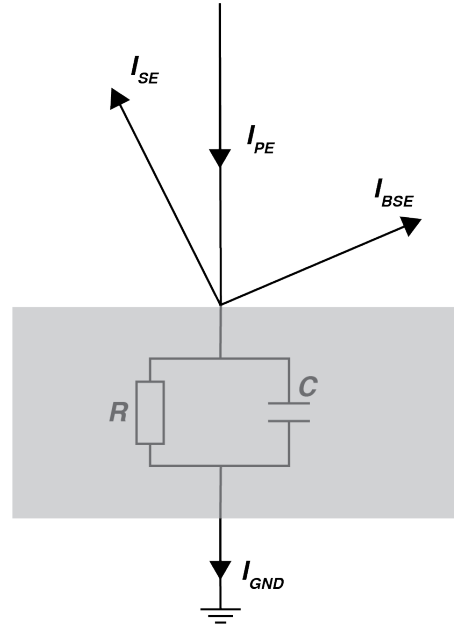

Figure 4.1: Impact of a primary electron (PE) beam on a sample that has resistance R and capacitance C, producing currents of back-scattered (BSE) and secondary electrons (SE), a current passing to ground (GND) and an accumulation of charge.

One major factor affecting the charge balance in Equation 4.1 is the speed at which the beam electrons strike the sample: electrons at higher accelerating voltages penetrate deeply into the sample and are less likely to escape. The penetration depth and, therefore, the landing energy at which the charge balance is achieved depends on the sample's composition (Reimer, 1998). For example, sections of Hard-Plus embedded samples already show charging while imaged with an electron beam at 1.5 keV landing energy and a secondary electron detector at 110 nm (Figure 4.2). Charging phenomena starts with image distortion arising from the incident electron beam being deflected. In the extreme case of very thick (500 nm non-conductive sections (Figure 4.4 b), anomalously stronger signal appears locally in the specimen, image contrast becomes low and it is impossible to have a high-resolution image of the surface. For sections thicker than 110 nm, finding another way to eliminate charging of the sample surface is important.
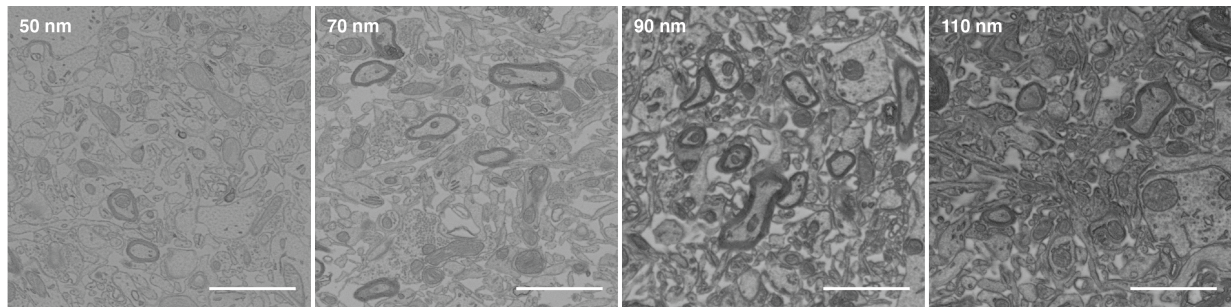

Figure 4.2: Imaging sections of varying thickness with an In-lens detector, primary electron beam 1.5 keV landing energy, 1.8 nA current and 400 ns pixel dwell time. The bar is 2 μm.

The simplest way to overcome charging problems is to coat the sample's surface with a very thin layer, even a few nanometres, of a conductive metal (Echlin, 2009), facilitating the flow of charge to ground. However, using this method in GCIB-based methods, mean coating each section and additionally mill the top metal coating at every milling cycle, significantly increasing milling times.

Alternatively, introducing positive ions in the EM vacuum chamber helps to neutralise the surface charge. Positive ions can be generated either by the electron beam passing through the low gas concentration at low vacuum (Robinson, 1975; Moncrieff et al., 1978) or with an ion gun (Crawford, 1979). Unfortunately, these methods are not compatible with imaging detecting low-energy secondary electrons.

Finally, sometimes it is possible to alter the chemical nature of the whole sample and convert it to a conductor (Echlin, 2009). For example, adding a conductive filler such as

carbon (Jia et al., 2002) to the epoxy polymer matrix improves the conductivity. However, the filler's size makes it impossible for it to spread throughout the whole sample volume. High energy (keV-MeV) ion irradiation of thin polymer films at high energy density alters the polymer's atomic and electronic structure, causing it to evolve into a more conductive amorphous carbon (Calcagno et al., 1992). (Hayworth et al., 2020) observed that charging of thin slices decreased with extended imaging and subsequently demonstrated that electron irradiation could be used to make sections even of $10\,\mu m$ thickness sufficiently conductive and smooth to allow quality In-Lens imaging and produce volume data. The dose of $5 \times 10^{26}\,eV\,cm^{-3}$ was sufficient to eliminate charging completely.

Furthermore, other physical properties, such as hardness, also see alteration (Lee et al., 1991). Since the milling rate of GCIB shows inverse proportionality to the hardness of the milled material (Yamada, 2016), it is expected to observe a decrease in the milling rate of irradiated samples in comparison to not irradiated.

4.2   Materials and Methods

Sample preparation and collection

The sections were cut from the sample with an ultramicrotome (Leica UC7, Leica Microsystems) and a diamond knife (DHJ4580, DiATOME), collected on square silicon wafers with dimensions 10 mm x 10 mm (J12006, Siegert Wafer).

Imaging

Imaging was performed using an In-lens detector of an SEM (Zeiss Merlin, Zeiss), the landing energy of the primary electron beams of 1.5 keV, probe current of 1.8 nA and 400 ns pixel dwell time. Focusing was done with a soon to be published algorithm, written by Rangoli Saxena.

4.3   Results and Discussion

In the original paper (Hayworth et al., 2020) that described the pipeline of the GCIB-SEM method, the authors used the electron beam of an electron microscope to irradiate the samples and induce their conductivity. This procedure is not optimal for large volume acquisition because of the limited field of view in the microscope and low incoming beam current. Therefore, it was important to have a stand-alone system to reliably induce conductivity in sections that are later processed in GCIB-mSEM.

Irradiation setup

To implement this setup, we purchased an electron gun (EH-50-3, Staib Instruments) that produces electron beams of energies ranging from 1 keV to 50 keV. The gun required a vacuum chamber to operate and a computer to configure the settings. Also, we deduced that we would need a digital multimeter to read the incoming electron current during the irradiation process. The setup is sketched in Figure 4.3.
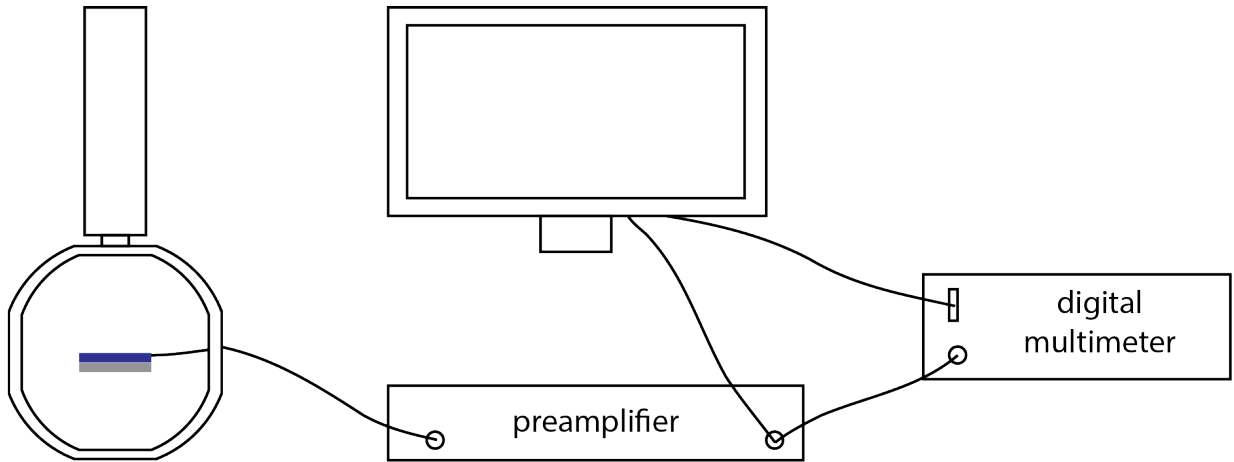

Figure 4.3: Sketch of a system for inducing conductivity in thick sections, that consists of an electron gun and a vacuum chamber, preamplifier, computer and digital multimeter. The vacuum chamber has an isolated stage that accommodates a wafer.

We used the top flange of a commercially available spherical cube vacuum chamber with six flanges (MCF600-SphCube-F6, Kimball Physics) to mount the electron gun. Two side flanges were used for mounting a turbo pump and a pressure sensor; both required confinement with lead lining to protect from possible X-rays generated by electrons with

energies above 30 keV. We used the third flange as a door with a static stage affixed onto which to place wafers. The fourth flange was reserved for a secondary electron detector.

We electrically isolated the sample wafer from the chamber with a sapphire wafer of the same size, also providing excellent heat conductivity. Thermal dissipation was needed to prevent overheating the sample that is embedded in epoxy with low-boiling point (at 180 °C) during high-energy electron irradiation. We connected the electrically isolated wafer to a wire that leads the sample current through a vacuum feedthrough to a preamplifier that amplifies and converts the low current signal to voltage (SR 570, Stanford Research Systems). The amplified voltage signal is then split between the digital multimeter (34465A, Keysight) and the voltage reading for imaging. Imaging was necessary for positioning the beam across the sample area while the multimeter reading monitored the irradiation dose. The resulting system can be seen in Figure 4.4 (a).
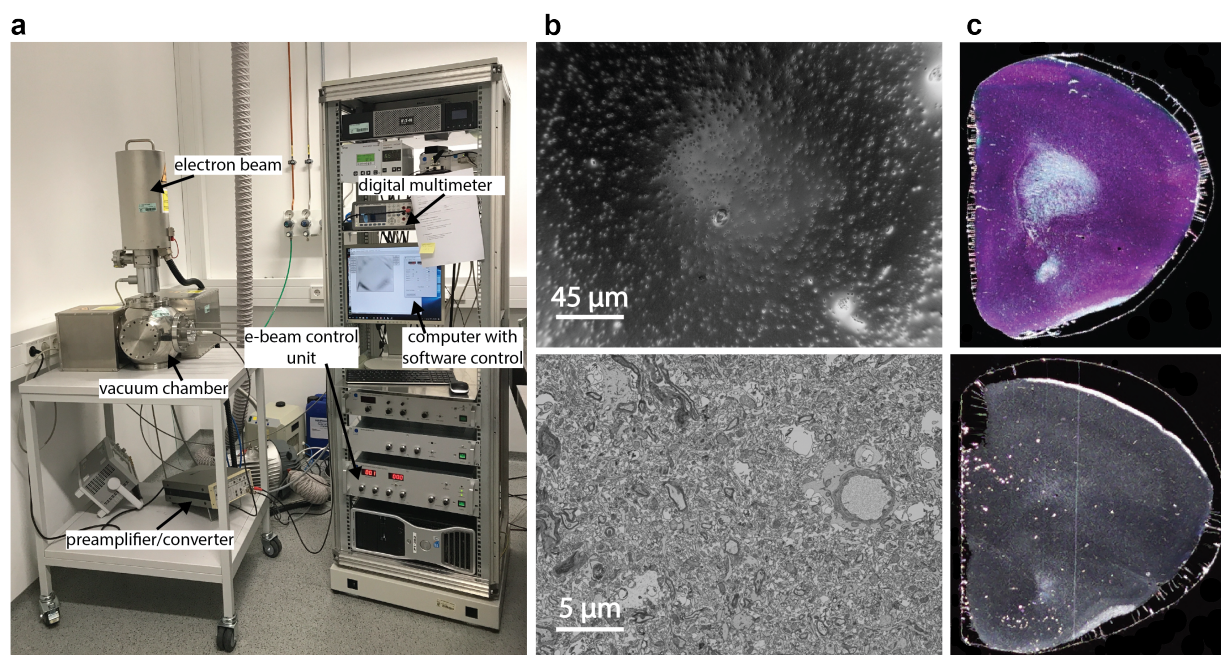

Figure 4.4: (a) Setup for radiation induced conductivity, consisting of an electron beam, a vacuum chamber, computer, multimeter and a preamplifier. (b, c) Example of 500 nm thick sections before (top) and after (bottom) irradiation imaged (b) in electron microscope with corresponding (c) optical images. The irradiation also caused the colour change of the sections in the optical image.

Irradiation can take a few hours, sometimes days, depending on the thickness of the sections and the area that they cover. Table 4.1 shows irradiation times for various areas

and thicknesses, assuming that the current is set to $30\,\mu A$. Therefore, we also set the goal to automate the irradiation system such that the dose can be monitored and the system switched off upon reaching a specified target. Unfortunately, Staib's electron gun's standard control and imaging software do not have such an option.

Thickness, nm	Energy, keV	Area, cm^2	
		2.5×2.5	5.0×5.0
100	1.5	31 h	124 h
250	3.5	33 h	133 h
500	6.0	39 h	155 h
1000	9.0	52 h	206 h

Table 4.1: Irradiation times of sections of various thicknesses and areas.

After a discussion with Staib Instrument's engineers, they provided us with information on how to send commands to the gun. Knowing this information, we found the dependency between sent bytes and the physical values and used the relationship to allow changing the settings of the gun from within our custom software, such as filament, energy, focus and grid parameters. Respecting Staib's confidentiality wishes we do not publish the details. We also automated the calculation of the dose and shutting off of the gun. For the user's convenience we created a graphical user interface via `wxPython`. Figure 4.5 shows the interface of the created software.

For proper calculation of the resulting dose, in addition to the gun parameters, the software needs to know the thickness of the sample, the irradiated area, and the current throughout the irradiation process. The thickness is set during collection of the sections and the irradiated area can be easily calculated from the raster voltage image in Staib's SEM software[1]. The incoming current can be converted from the voltage read out from the digital multimeter knowing the chosen sensitivity of the preamplifier. With all the parameters known, the dose at a time of a measurement D_T can be found as following:

$$D = \frac{E}{S \cdot h \cdot q} \int I(t)\, dt \qquad (4.2)$$

Where E and $I(t)$ are the energy and the current of the incident electron beam, S and h are the irradiated area and the thickness of the samples, q is the elementary charge and

---

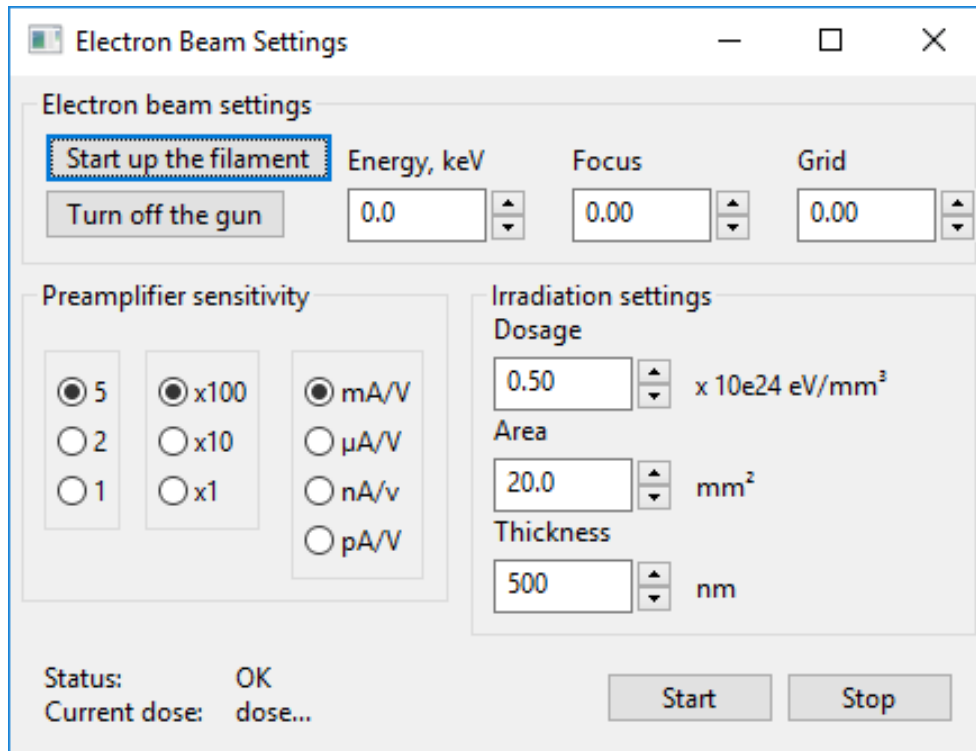[1]https://www.staibinstruments.com/products/data-acquisition-and-instrument-controls/

Figure 4.5: GUI for the irradiation system software

t is time. The integral in Equation 4.2 can be approximated with a Riemann sum:

$$D = \frac{E}{S \cdot h \cdot q} \sum_i I_i \Delta t_i \tag{4.3}$$

The software calculates the dose at intervals of 5 seconds.

Using this system we could consistently get conductive samples irrespective of thickness and area. The sections also showed a difference in their appearance (Figure 4.4 c), becoming grey, confirming the change in their atomic structure. With higher conductivity, we could obtain images at higher resolution and resolve small processes in the micrograph (Figure 4.4 b).

Beam energy vs. section thickness

The appropriate beam energy must be used during irradiation to ensure that the electrons affect the whole volume of each section. In the original paper (Hayworth et al., 2020) that described the pipeline of the GCIB-SEM method, the authors presented estimated optimal electron energy for irradiation with energy resolution enough for thick sections.

Our sections being much thinner, required estimates at a finer scale. To that end, we used Monte Carlo modelling software (Drouin et al., 2007) that simulates electron trajectories in the epoxy. We used the tool to create energy density plots for a wide electron beam with energies ranging from 1 keV to 10 keV irradiating an epoxy block with 0.02 Osmium atomic fraction. The atomic fractions of C, O and H in epoxy were determined to preserve the typical C:O:H ratio of epoxy and match the density of Hard-Plus Resin-812. Figure 4.6 shows the average penetration depth over 20000 electrons for each tested electron energy where energy density drops to 25% of the initial value. From this graph, the necessary energy setting for the gun can be obtained.
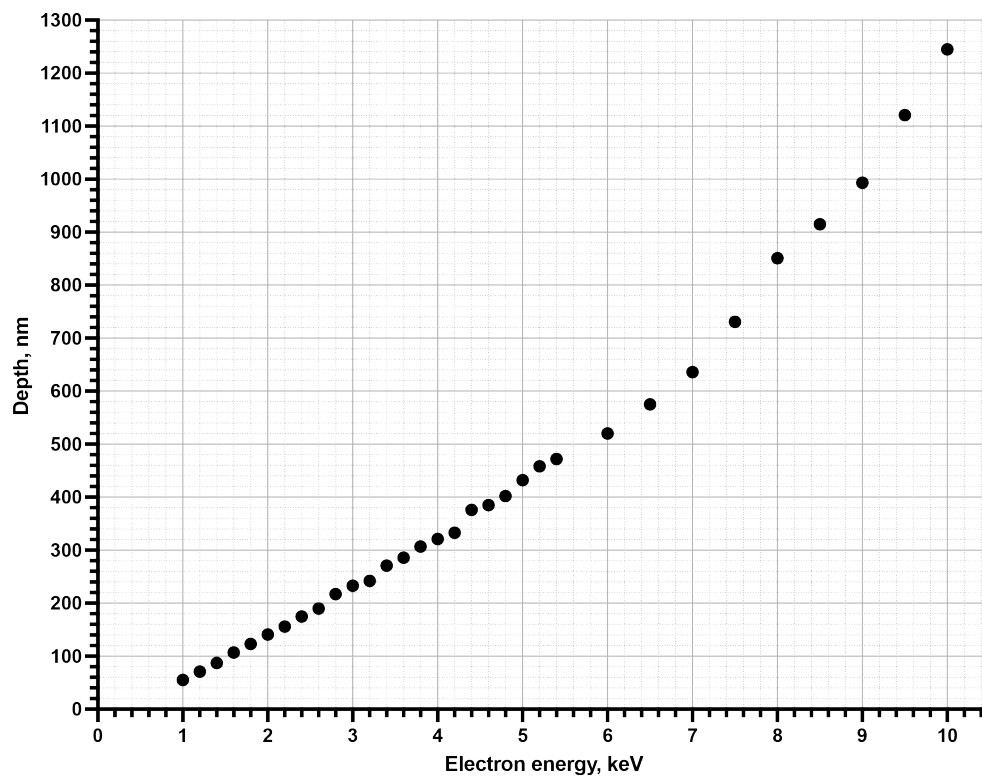

Figure 4.6: Dependency of penetration depth on electron energy for energies between 1 keV and 10 keV

4.4   Summary

We designed and build an irradiation system and wrote corresponding software to set up and automate the irradiation of samples. Specifically, the software includes functionality to properly start up the filament without supervision, to turn off the gun manually or upon reaching the target dose. Also, the software states the status of the hardware, be it in the process of starting up the filament, irradiating the sample or ready to receive commands. In addition, it displays and updates the irradiation dose every 5 seconds.

The system reliably induces conductivity in epoxy-embedded sections that provides tissue contrast in secondary electron imaging.

For the user's convenience, a graph for looking up the appropriate irradiation beam energy for semi-thin sections was plotted.

Chapter 5

Gas Cluster Ion Beam Milling

The sample preparation method for mSEM-GCIB allows for processing multiple wafers at the same time. The ideal GCIB-mSEM system can image and mill wafers in parallel with neither being a bottleneck. With this in mind, the mSEM image acquisition rate sets a high bar for GCIB milling. However, a higher milling rate should not degrade the ability of the system to produce a smooth surface — a requirement for high-resolution imaging and the tracing of small processes in the brain. Thus, this chapter explores the parameters of the GCIB milling of Hard-Plus embedded samples.

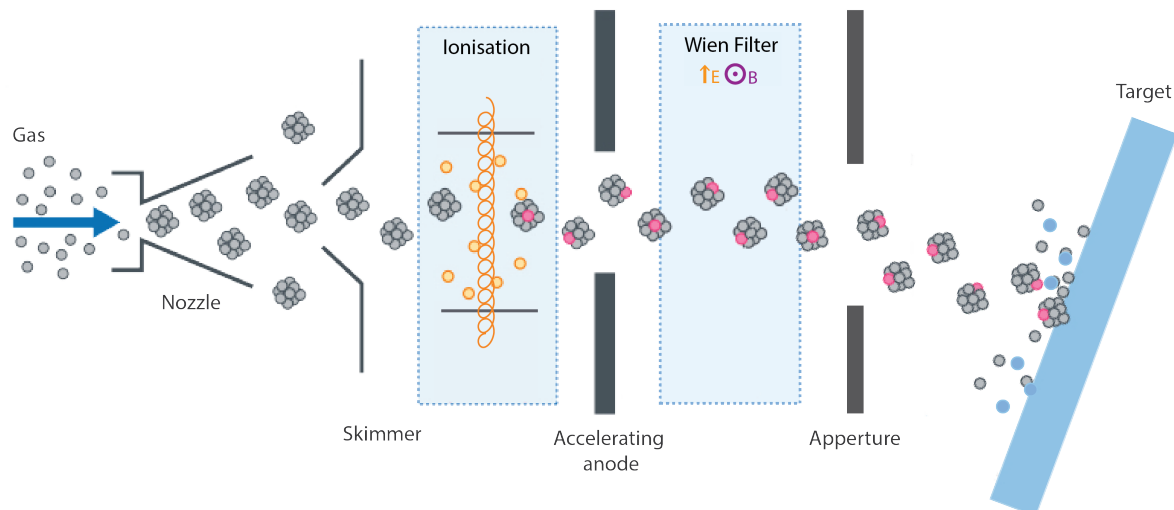# 5.1   Introduction

Gas Cluster Ion Beam

Figure 5.1: Typical configuration of gas cluster ion beam

A possible solution to the mechanical problems of SBEM and the limits of FIB-SEM imaged volumes would be using a gas cluster ion beam (GCIB) for milling samples. GCIB processing of materials is based on the use of electrically charged accelerated cluster ions consisting of a few hundred to a few thousand atoms or molecules of gaseous materials.

A typical GCIB system (Figure 5.1) usually has three vacuum chambers: a nozzle chamber, an ionisation/acceleration chamber and a target chamber. In the nozzle chamber, neutral gas clusters are formed by expanding the source gas at high pressure through a supersonic nozzle into a vacuum. Depending upon the application, clusters can be produced from various gases, including Ar, O_2 or N_2. The directed axial stream of clusters emerging from the nozzle passes through an aligned skimmer. Clusters passing through the skimmer to the second vacuum stage are ionised by electron bombardment and then accelerated with an anode voltage. As the resulting charged gas cluster beam consists of a distribution of different cluster sizes, selecting only the needed clusters for milling is important. This is achieved by introducing a Wien filter that helps select the accelerated charged clusters of a certain mass.

Ionoptika 10S system

The Ionoptika 10S system is a gas cluster ion beam source that delivers ions of energies up to 10 keV and has selectable clusters from 1 to 3000 atoms per cluster. The resulting spot size is large and the source has a wide scan field. The software provides sample current reading, and imaging with either sample current or with a secondary electron detector.

We used of Corgon gas to create clusters, that consists of 82% argon and 18% carbon dioxide. The upgrade to the standard system included a modified expansion nozzle and an enlarged Wien filter aperture that resulted in the increase of beam current.

Sputtering and smoothing of the surface

The bombardment effects of monomer ions and large cluster ions are very different, even at the same energy per atom. When an accelerated cluster ion hits a solid surface, the impacted area experiences both high temperature and high pressure transients that produce vaporisation of both target and projectile materials. Monomer ions do not produce an equivalent phenomenon due to the binary collision nature of the interaction with the target and do not introduce similarly high-energy densities into the impact volume. Simulation results (Yamada, 2016) indicate that in the cluster impact, many particles are sputtered with directions lateral to the trajectory of the impinging cluster and causing the formation of craters. The shape of the craters has been determined to be hemispherical with a radius that can be predicted according to several empirical relations, one of them being the following (Kinslow, 1970):

$$\frac{h}{D_p} = K \left(\frac{\rho_p}{\rho_t}\right)^{\frac{2}{3}} \left(\frac{v_p}{c}\right)^{0.58}, \tag{5.1}$$

where h is the crater depth, D_p is the diameter of the projectile, K is a numeric constant, ρ_p and ρ_t are the projectile and target densities respectively, and v_p and c are the projectile and sound velocities. From the formula, the resulting crater depth can be estimated to be in the order of a tenth of a nanometer. The GCIB smoothing process may be considered as a stochastic overlaying of many such shallow craters from the individual impacts of clusters.

GCIB is highly effective at removing surface asperities and has already been successfully applied for smoothing surfaces of various materials (Bourelle et al., 2005; Insepov et al., 1998). Though, only certain epoxides and only certain angles show the characteristic smoothing role of GCIB in the case of brain tissue (Hayworth et al., 2020). Therefore, it

was important to investigate whether Hard-Plus resin's use in brain tissue preparation was suitable for GCIB milling.

5.2   Materials and Methods

Sample preparation and collection

The sections were cut from the sample with an ultramicrotome (Leica UC7, Leica Microsystems) and a diamond knife (DHJ4580, DiATOME), collected on square silicon wafers with dimensions 10 mm x 10 mm (J12006, Siegert Wafer). All sections had a thickness of 500 nm.

For 500 nm thick sections, the acceleration voltage was set to 6 keV (Figure 4.6, chapter 4) in the irradiation setup and the sections were irradiated to the dose of 5×10^{26} eV cm^{-3}.

Imaging

Imaging was performed in a field emission SEM (Zeiss Merlin, Germany) using an In-lens detector, the the acquisition process was automated using the open-source software SBEMimage[1] (Titze et al., 2018). The acceleration voltage of the electron beam was set to 1.5 keV, probe current of 1.8 nA and 400 ns pixel dwell time. Focusing was done with a soon to be published algorithm, written by Rangoli Saxena.

Aligning the volumes

The image stack is aligned using the SIFT (Lowe, 2004) tool within Fiji software[2].

Milling rate calculation

The milling rate can be calculated by dividing the volume that has been milled by the time taken. The amount of tissue that has been milled can be determined via two methods.

First method: Direct calculation

First, since the milling time at each milling cycle is the same, one can assume that the amount of tissue milled during each cycle is also identical. Hence, the thickness that has been milled at each cycle can be found by dividing the section thickness by the total number of cycles taken to mill away the whole section.

---

[1]https://github.com/SBEMimage
[2]https://imagej.net/software/fiji/

Second method: Pixel intensity jump estimation

Second, similar to the section-to-section loss estimation in Hayworth et al. (2020) by calculating a difference matrix. An image with a known pixel size from the same sample as the one under investigation is first smoothed with a 2D Gaussian filter (r=4 pixels), and then a matrix of mean pixel-by-pixel line differences is calculated across the whole image. Averaging those entries with equal distance between pixels enables the dependency of change in grey-scale against distance to be plotted. Assuming this relationship holds along the z-axis, the total material milled can then be calculated from the grey-scale jump along the z-axis.

5.3   Results and Discussion

Experimental setup of single-beam SEM - GCIB

To allow for a higher milling rate, we asked the company Ionoptika, the producer of our GCIB columns, to modify the system to achieve a current higher than the advertised 10 nA. They provided a modified expansion nozzle and an enlarged Wien filter aperture which resulted in a 60 nA current. To test the upgraded GCIB and establish milling capability and rates for Hard-Plus embedded samples, we mounted the GCIB gun (GCIB 10-S, Ionoptika) to an SEM (Zeiss Merlin, Zeiss). During the aqusition proccess, the stage, together with the specimen is moved between two positions: imaging and milling. Imaging position was located at 4 mm working distance from the electron column and the milling position is at the centre of the ion beam, tilted to a chosen incident angle. To achieve uniform material removal, the sample is constantly rotated, so milling occurs from multiple directions.

Determination of GCIB parameters

Before starting the experiments, we determined the configuration parameters for GCIB gun. The Ionoptika GCIB specification allows for acceleration voltages be up to 10 keV and the cluster size between 1 and 5000. The goal is to identify the parameters for a faster milling.

Assuming that the beam current and target tissue are held constant, the milling rate ultimately depends on the depth of the crater each cluster makes. The greater the depth of a crater, the higher the milling rate. The equation Equation 5.1 for crater's radius h can be simplified to a relation:

$$h \propto v_p^{0.58} D_p, \tag{5.2}$$

since K, ρ_p, ρ_t and c are independent of cluster energy and size.

Velocity of the projectile is linearly proportional to the square root of its kinetic energy divided by the mass: $v_p \propto \sqrt{\frac{E}{m}}$. The mass, in turn, is linearly proportional to the cluster size N, hence:

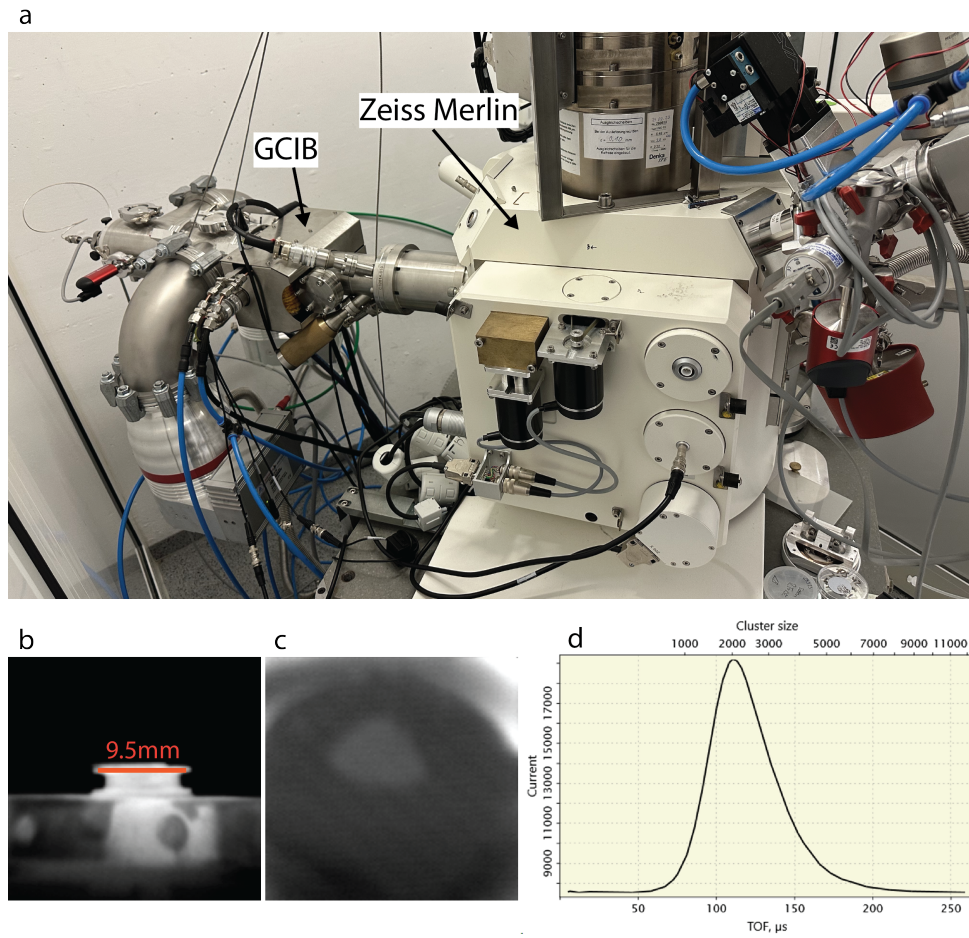$$v_p \propto \sqrt{\frac{E}{N}}. \tag{5.3}$$

Figure 5.2:   (a) Experimental setup of single beam EM and GCIB. Panels (b) and (c) are current images of the sample holder with a sample on it. Panel (d) shows the distribution of the cluster sizes in the resulting beam measured via the time-of-flight method.

The diameter of the projectile D_p can be approximated as

$$D_p \approx \sqrt[3]{\frac{6V_p}{\pi}}, \tag{5.4}$$

where volume V_p of the projectile is proportional to the cluster size, therefore:

$$D_p \propto \sqrt[3]{N}. \tag{5.5}$$

Combining equations Equation 5.2, Equation 5.3, Equation 5.5:

$$h \propto E^{0.26} N^{0.07}. \tag{5.6}$$

It follows that the milling rate would depend both on the energy and size of the clusters, with, of the two, the change in energy having the larger effect due to its comparably higher power. The Ionoptika gun can deliver a maximum of $10\,\text{keV}$, therefore, that was the chosen energy for the experiments. One cannot, however, increase the cluster size indefinitely, as there is a threshold energy per atom $\frac{E}{N}$ required to cause displacement in the target and hence sputtering of the target material (Yamada, 2016). It was established experimentally that for $10\,\text{keV}$ acceleration, there was no damage or displacement in the target sample beyond argon cluster size $N = 3000$. To ensure that most clusters are close to but smaller than this size, the distribution mean was set to around 2000. The distribution can be seen in Figure 5.2 d.

Milling rate and surface quality dependencies on milling angle

Apart from the beam current, energy and cluster size, the glancing angle of the beam also plays a role in milling outcome. To test the milling angles, we collected sections from a sample onto separate wafers, irradiated them to the same dose. Then, we acquired a volume stack of those images keeping the imaging conditions the same. We kept milling field of view the same through out all of the experiments, the only difference was the milling glancing angle.

Figure 5.3 shows the milled surfaces of those samples at 40°, 30°, 20° angles. The 40° milling yields a rough surface which makes it harder to produce well-focused images and trace small processes, if any at all.
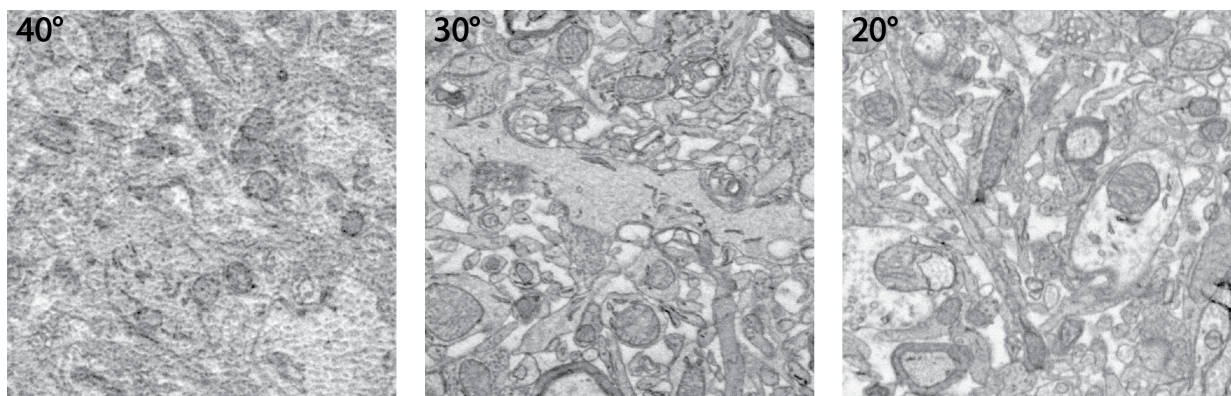

Figure 5.3: Surface quality after milling at 40°, 30°, 20°.

Milling rate for each glancing angle was calculated after finding the amount of tissue

being milled per cycle. Since milling in the case of 40° did not produce a smooth surface, we calculated the milling thickness by dividing the original slice thickness by the number of imaging cycles. Conversely, for 30° and 20° we additionally used the similarity matrix method.
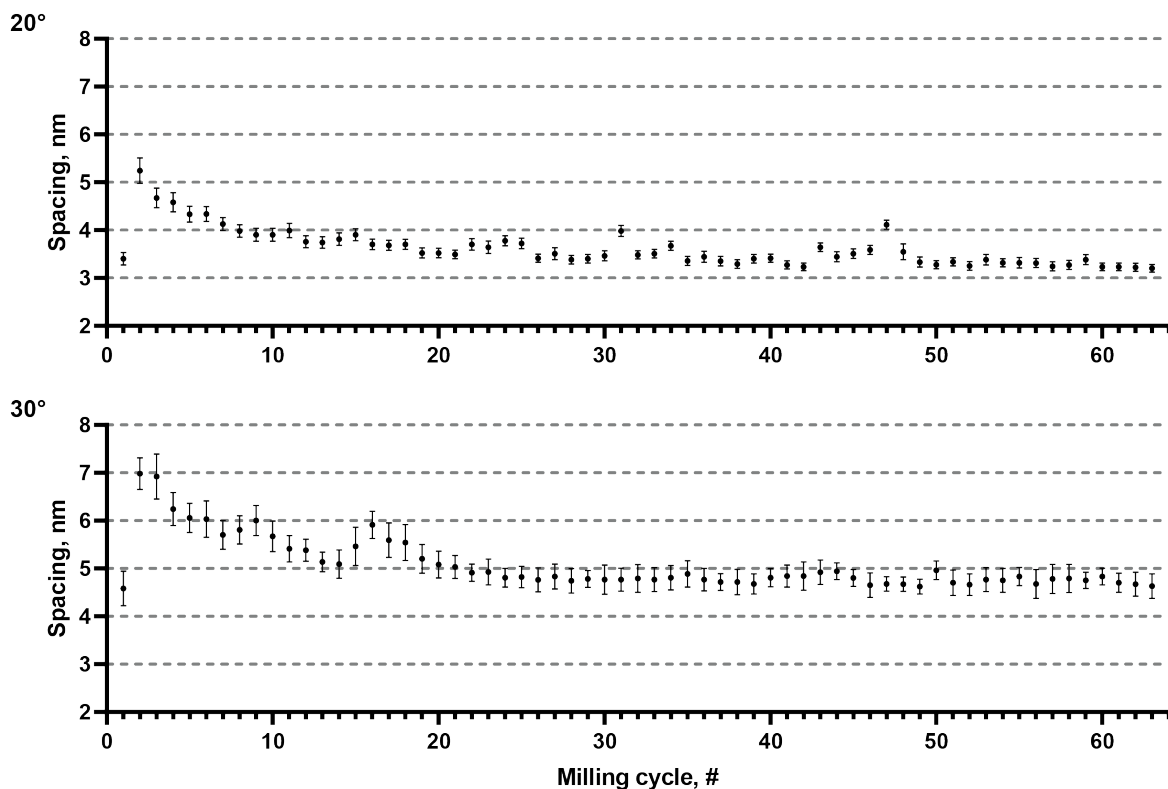

Figure 5.4: Calculation of milling spacing over the first 64 milling cycles for millings at (top) 20° and (bottom) 30°

The estimated depth milled with each successive iteration can be seen in Figure 5.4. The jump between the first and second imaging is attributed to a difference in imaging the top oxidised layer and the consecutive milled layer, that has not been oxidised. After this sudden change, the milled quantity steadily decreases and stabilises at some point. We reason this is due to the irradiation caused by the electron beam during imaging, further increasing the irradiation dose and, therefore, hardness, hence decreasing the milling rate. Penetration depth of a beam with energy 1.5 keV, at which imaging happens, is around 100 nm (Figure 4.6). We should consequently expect, each milling cycle within the

first 100 nm to encounter a more irradiated section due to accumulated radiation during successive imaging cycles (Figure 5.5 a). Beyond the first 100 nm, however, each layer of the remaining tissue volume will have been exposed to an equal amount of extra radiation, leading the milling rate to stabilise.

Having identified the depth of tissue milled during a milling cycle z, we could calculate the milling rate M:

$$M = \frac{S_{FOV} \cdot z}{\sin \alpha \cdot t} \tag{5.7}$$

Milling time, t, is defined by the duration of one milling cycle. The milling area, S, can be calculated from the area of the ion current image S_{FOV} (Figure 5.2 b-c) in the Wien Filter software from Ionoptika by taking into account the milling angle α.

Milling angle	Milling cycles, amount	Spacing, nm		Milling rate, $\mu m^3 s^{-1}$	
20°	148	2.6[1]	3.5[2]	422[1]	568[2]
30°	105	4.8[1]	5.1[2]	533[1]	566[2]
40°	33	6.7[1]	NA	579[1]	NA

Table 5.1: Milling rates calculations depending on angle

1 - calculated using the first method
2 - calculated using the second method

Table 5.1 summarises, for each milling angle, the resulting slice thicknesses found with each method and estimated milling rates. We suppose this discrepancy is due to non-uniformity in milling rate across the sample; evident in substrate breakthrough at different z-planes (Figure 5.5 b). Due to the nature of the similarity matrix based method, the inconsistencies due to more slowly milled regions average out as there are so few of them in comparison to total sample volume. However, when dividing sample thickness by total number of cycles, the more slowly milled regions of the sample bias the calculation towards a lower spacing, as they extend the total number of cycles passed the average across the sample as a whole. It is this rate, however, which is important for total acquisition time, as we must wait for the entire sample to be milled.

This relationship between milling rate and sample smoothness for different milling angles suggests a trade-off. Increasing the angle increases the milling rate, but also, passed a certain point, results in images of degraded quality. Out of the three angles tested, a glancing angle of 30° shows the best trade-off.

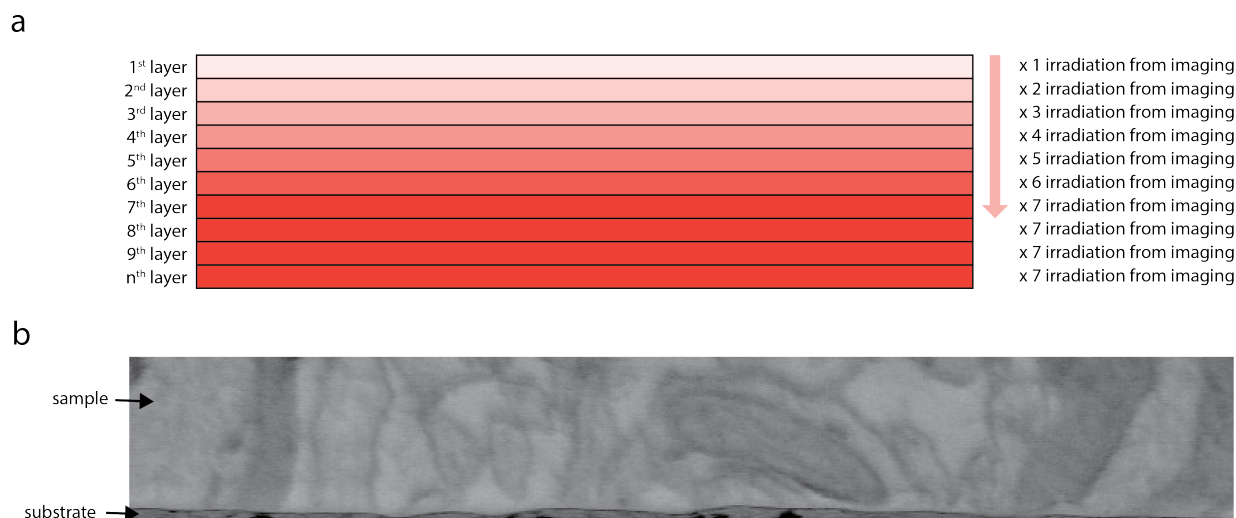Given this result, we calculated milling times to ensure they were no longer the bot-

a

1st layer	x 1 irradiation from imaging
2nd layer	x 2 irradiation from imaging
3rd layer	x 3 irradiation from imaging
4th layer	x 4 irradiation from imaging
5th layer	x 5 irradiation from imaging
6th layer	x 6 irradiation from imaging
7th layer	x 7 irradiation from imaging
8th layer	x 7 irradiation from imaging
9th layer	x 7 irradiation from imaging
nth layer	x 7 irradiation from imaging

b

sample →

substrate →

Figure 5.5: Explanation of milling rate variation. (a) Accumulation of additional electron irradiation during imaging. In the example, the landing energy of the primary electrons allows for penetration up to a depth equivalent to 7 layers. Starting from the 7th layer, all subsequent layers have the same additional accumulated electron irradiation dose causing the milling rate to stabilise. (b) The cross-section of an acquired image stack, showing that the substrate is reached during earlier cycles across most of the section, with only small areas still requiring a few additional milling cycles (in this case, 6 more) to image the whole volume.

tleneck in the acquisition process. For a 2-inch wafer ($R = 50.8\,\mathrm{mm}$) that is fully covered with slices with z-spacing of $10\,\mathrm{nm}$ the total time is:

$$t_{mill} = \frac{S \cdot z}{M} = \frac{\pi \cdot R^2 \cdot z}{M} = \frac{\pi \cdot (25.4\,\mathrm{mm})^2 \cdot 10\,\mathrm{nm}}{533\,\mathrm{\mu m^3\,s^{-1}}} \approx 10\,\mathrm{h} \qquad (5.8)$$

Comparing this with the result in Equation 1.3 for imaging which came to $24\,\mathrm{h}$, we see there is now in fact potential to increase the imaging speed in the parallelised GCIB-mSEM system. Further increases in acquisition rate could be achieved by increasing the contrast of the samples by improving the staining procedure.

Setup combining GCIB and mSEM

With all the necessary parameters identified, we built an mSEM-GCIB system, wherein a custom-made additional vacuum chamber for milling was attached to the existing mSEM chamber (Figure 5.6, Figure 5.7). The chambers are isolated via a pneumatic gate valve.

A specially designed robotics arm with three degrees of freedom — horizontal, vertical and rotational about the horizontal axis — transfers the wafers between the imaging and milling chambers. The GCIB is mounted on top of the milling chamber. The chamber encompasses an x-y stage mounted at a fixed 30° glancing angle towards the GCIB, on top of which, is an additional stage which supports 360° rotation to allow for uniform milling. To enable exchange when simultaneously processing two wafers, we have another parking place for a second wafer within the milling chamber. The manual gas and column valves were substituted with pneumatic valves for automation purposes.

The GCIB current is around 75 nA with a peak at 2000 atoms per cluster.
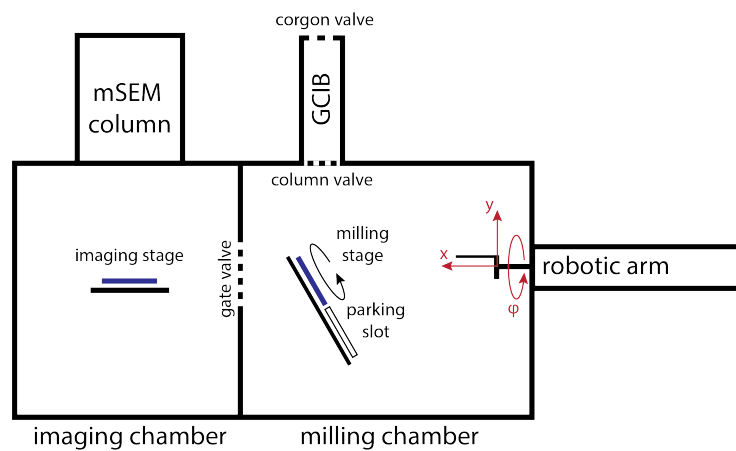
Figure 5.6: Schematics of GCIB-mSEM system

During experimental runs of the system, we noticed that a continuous supply of the gas to the milling chamber disturbs the mSEM beams when the gate valve is open. Therefore, we ensured that the supply of Corgon into the chamber is switched off when we open the gate valve for transferring the wafers between the chambers. However, we observed that constantly using the column valve to stop Corgon from coming into the milling chamber significantly decreases the filament life. Instead, we close the gas valve and then wait a time for the Corgon to evacuate from the chamber and only then open the gate valve between the milling and imaging chambers. The column valve is closed only when the Corgon valve is off and the filament is cooled down.

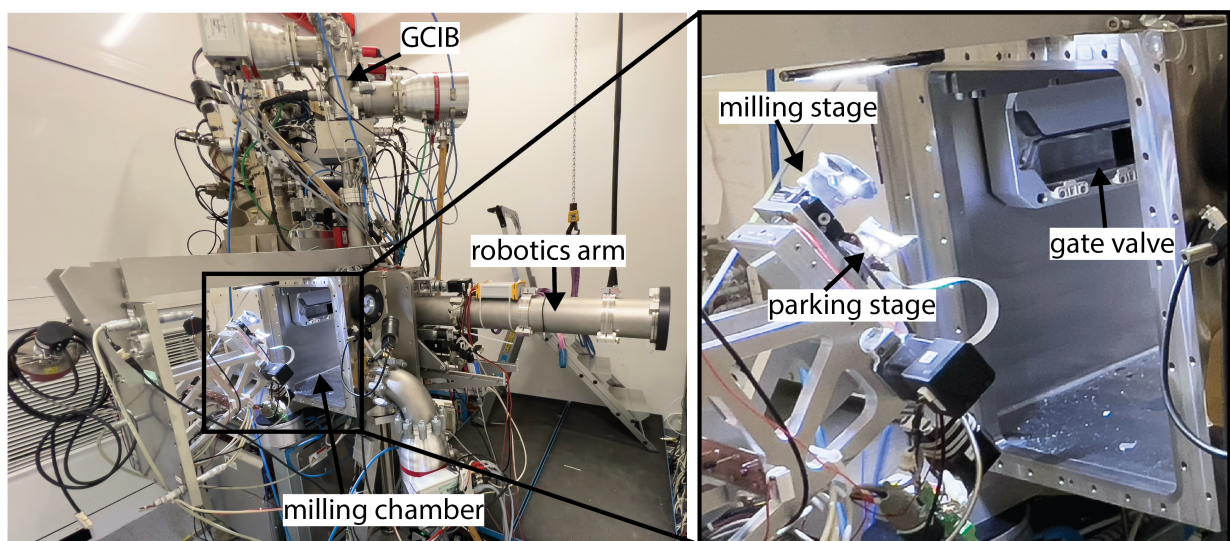The development of software for complete automation is still ongoing.

Figure 5.7: GCIB-mSEM system. In the foreground of the left image is the milling chamber with the GCIB gun mounted on top and the robotic arm on the side. On the right is a close-up of the milling chamber showing the gate valve and the milling and parking stages.

5.4   Summary

Described in this section, was the experimental setup we used for the identification of GCIB milling parameters of Hard-Plus embedded samples. The use of Hard-Plus resin was motivated both by its ability to infiltrate large tissue volumes and its excellent cutting qualities (chapter 2). Our goal was to maintain a smooth surface during milling allowing for high-resolution imaging and identification of small processes in the brain, while also providing a high enough milling rate to keep up with imaging in the mSEM.

We established milling parameters and showed that our setup exceeds the necessary milling rate required to maintain pace with imaging at a glancing angle of 30° while also providing a smooth surface.

Ultimately, this means we can build a GCIB-mSEM system that can acquire two wafers simultaneously. If, however, the image acquisition rate significantly improves, there would again be a need to increase the milling rate.

Chapter 6

Conclusion and Outlook

To test our pipeline for large field-of-view volume acquisition with GCIB-mSEM, I first established a staining protocol for whole-coronal cross-sections of a mouse brain that produced high contrast when imaged with an In-lens detector in an SEM. However, more work is needed to develop a whole mouse brain staining protocol free of artifacts. Additionally, Hard-Plus Resin was tested and determined suitable for the infiltration of large volumes and was found to have superior cutting quality compared to Spurr's.

For sectioning, we customised the existing ultramicrotomes to allow for time- and location-based separation of cutting and collection. Although locational separation increases the amount of sections that can be collected on the wafer, this method still needs improvement to allow for automation and reliable transfer through the channel.

We designed and built an electron beam irradiation system to induce conductivity in collected sections for SEM imaging. We then completely automated it with custom software. Th system can be used for the routine preparation of collected sections for the large field-of-view GCIB-mSEM based acquisition system, providing irradiation rates fast enough, so as to not bottleneck the acquisition.

We built an SEM-GCIB system to determine the milling parameters. Hard-Plus embedded tissue was shown to maintain a smooth surface after milling at small glancing angles. Using this system, we identified the milling parameters and verified and tested that the milling of wafers can keep up with the imaging rate in the mSEM while maintaining adequate quality. The imaging rate could be increased by further improving staining contrast. Depending on the degree of this increase, one might have to further speed up the milling.

Overall, the calculated time required for the whole mouse brain acquisition with the

faster imaging and/or parallelisation of the acquisition across multiple GCIB-mSEM systems seems feasible for acquiring the whole mouse brain.

All things considered, we built a system combining the GCIB and the mSEM and are on our way to automate the acquisition process with custom software. The software, among other features, includes automated normalisation of wafer images and both manual and automated modes of boundary point collection in addition to functionality for mSEM stage positioning via the corresponding optical image of the wafer.

Appendix A

List of Abbreviations

ECS   Extracellular space

ACSF   Artificial cerebrospinal fluid

CB   Cacodylate buffer

TCH   Thiocarbohydrazide

SEM   Scanning Electron Microscopy

mSEM   Multi-beam Scanning Electron Microscopy

BSE   Back-scattered electrons

SE   Secondary electrons

GCIB   Gas Cluster Ion Beam

Appendix B

Heavy metal staining protocol for biological tissue

Mice were decapitated and the brain was then swiftly dissected, and slices of $500\,\mu m$ were cut at 4°C on a vibratome (VT1200 S, Leica) in ACSF. Slices were then transferred into a fixative solution for an overnight fix at 4°C and subsequently rinsed with $200\,mM$ CB buffer five times over at least two days.

The first step in the staining procedure was to transfer the brain slice to a $20\,ml$ glass scintillation vial filled with a solution containing $80\,mM$ OsO_4, $70\,mM$ $K_4Fe(CN)_6$ and $200\,mM$ CB. After 1.5 hours, the slice was thoroughly rinsed three times with $200\,mM$ CB. Each time for 10-15 minutes. Then, the slice was immersed in the aqueous pyrogallol solution. After 1 hour, the slice was rinsed three times with water. Each time for 10-15 minutes. Then, the slice was transferred to an unbuffered aqueous solution of $80\,mM$ OsO_4 and kept there for 1.5 hours, after which it was again rinsed in water three consecutive times for 10-15 minutes. The slice was then transferred to a filtered 1% UA solution and left at 4°C overnight. The following morning, the slice was rinsed in water three times, with each rinse lasting 10-15 minutes and then they were transferred to Walton's solution (Walton, 1979).

The dehydration incubations were 30 minutes each, and the concentrations (all v/v) were 50%, 75% and 95% ethanol balanced with water followed by two times 100% of absolute dry ethanol from a freshly opened bottle and three times 100% of acetone from a freshly opened bottle as well. Each infiltration incubation of 25%, 50%, and 75% acetone balanced with epoxy was 48 hours long except for 100%, which was changed twice during the 48 hours.

For epoxy polymerisation, the brain slices were placed into a custom-made rectangular silicone mould with dimensions $18\,\text{mm} \times 10\,\text{mm} \times 7\,\text{mm}$ and cured at 70°C for 12 h.

Bibliography

Ann Ellis, E. (2018). Solutions to the Problem of Substitution of ERL 4221 for Vinyl Cyclohexene Dioxide in Spurr Low Viscosity Embedding Formulations. *Microscopy Today*, *14*(4), 32–33.

Birbeck, M. S. C., & Mercer, E. H. (1956). Applications of an epoxide embedding medium to electron microscopy. *Journal of the Royal Microscopical Society*, *76(4)*, 159–161.

Blumer, M. J., Gahleitner, P., Narzt, T., Handl, C., & Ruthensteiner, B. (2002). Ribbons of semithin sections: an advanced method with a new type of diamond knife. *Journal of Neuroscience Methods*, *120*(1), 11–16.

Bourelle, E., Suzuki, A., Sato, A., Seki, T., & Matsuo, J. (2005). Sidewall polishing with a gas cluster ion beam for photonic device applications. *Nuclear Instruments and Methods in Physics Research Section B: Beam Interactions with Materials and Atoms*, *241*(1), 622–625. The Application of Accelerators in Research and Industry.

Briggman, K. L., & Bock, D. D. (2012). Volume electron microscopy for neuronal circuit reconstruction. *Current Opinion in Neurobiology*, *22*(1), 154–161. Neurotechnology.

Burke, C., & Geiselman, C. W. (1971). Exact anhydride epoxy percentages for electron microscopy embedding (Epon). *Journal of Ultrastructure Research*, *36*(1), 119–126.

Calcagno, L., Compagnini, G., & Foti, G. (1992). Structural modification of polymer films by ion irradiation. *Nuclear Instruments and Methods in Physics Research Section B: Beam Interactions with Materials and Atoms*, *65*, 413–422.

Canny, J. (1986). A computational approach to edge detection. *IEEE Transactions on Pattern Analysis and Machine Intelligence*, *PAMI-8*(6), 679–698.

Couve, E. (1986). Controlled mounting of serial sections for electron microscopy. *Journal of Electron Microscopy Technique*, *3*(4), 453–454.

Cragg, B. (1980). Preservation of extracellular space during fixation of the brain for electron microscopy. *Tissue and Cell*, *12*, 63–72.

Crawford, C. K. (1979). Charge neutralization using very low energy ions. *SEM Inc.*, *60666*(17), 31–46.

Denk, W., & Horstmann, H. (2004). Serial block-face scanning electron microscopy to reconstruct three-dimensional tissue nanostructure. *PLOS Biology*, *2*, e329.

Doty, R. W. (2007). Alkmaion's discovery that brain creates mind: A revolution in human knowledge comparable to that of Copernicus and of Darwin. *Neuroscience*, *147*(3), 561–568.

Drouin, D., Couture, A. R., Joly, D., Tastet, X., Aimez, V., & Gauvin, R. (2007). CASINO V2.42—A fast and easy-to-use modeling tool for scanning electron microscopy and microanalysis users. *Scanning*, *29*(3), 92–101.

Dykstra, J., & Reuss, L. E. (2003). *Biological electron microscopy: theory, techniques, and troubleshooting*. New York: Kluwer Academic/Plenum Publishers.

Eberle, A., Mikula, S., Schalek, R., Lichtman, J., Tate, M. K., & Zeidler, D. (2015). High-resolution, high-throughput imaging with a multibeam scanning electron microscope. *Journal of Microscopy*, *259*(2), 114–120.

Echlin, P. (2009). *Handbook of Sample Preparation for Scanning Electron Microscopy and X-Ray Microanalysis*. New York: Springer.

Finger, S. (1994). *Origins of Neuroscience: A History of Explorations into Brain Function*. United Kingdom: Oxford University Press.

Fisch, W., & Hofmann, W. (1954). Über den härtungsmechanismus der äthoxylinharze [german]. *Journal of Polymer Science*, *12*(1), 497–502.

Fisch, W., Hofmann, W., & Koskikallio, J. (1956). The curing mechanism of epoxy resins. *Journal of Applied Chemistry*, *6*(10), 429–441.

Genoud, C., Titze, B., Graff-Meyer1, A., & Friedrich, R. W. (2018). Fast homogeneous en bloc staining of large tissue samples for volume electron microscopy. *Frontiers in Neuroanatomy*, *12:76*.

Glauert, A. M. (1975). *Fixation, Dehydration and Embedding of Biological Specimens.* North-Holland, New York: Elsevier Science.

Glauert, A. M., Glauert, R. H., & Rogers, G. E. (1956). A new embedding medium for electron microscopy. *Nature*, *178(4537)*, 803.

Harreveld, A. V., & Malhotra, S. K. (1967). Extracellular space in the cerebral cortex of the mouse. *Nature Methods*, *101(Pt. 2)*, 197–207.

Hayat, M. A. (2000). *Principles and Techniques of Electron Microscopy. Biological Applications.* United Kingdom: Cambridge University Press.

Hayworth, K. J., Kasthuri, N., Schalek, R., & Lichtman, J. W. (2006). Automating the collection of ultrathin serial sections for large volume tem reconstructions. *Microscopy and Microanalysis*, *12*, 86–87.

Hayworth, K. J., Peale, D., Januszewski, M., Knott, G. W., Lu, Z., Xu, C. S., & Hess, H. F. (2020). Gas cluster ion beam sem for imaging of large tissue samples with 10 nm isotropic resolution. *Nature Methods*, *17*, 68–71.

Hayworth, K. J., Xu, C. S., Lu, Z., Knott, G. W., Fetter, R. D., Tapia, J. C., Lichtman, J. W., & Hess, H. F. (2015). Ultrastructurally smooth thick partitioning and volume stitching for large-scale connectomics. *Nature Methods*, *12*, 319–322.

Hildebrand, D. G. C., Cicconet, M., Torres, R. M., Choi, W., Quan, T. M., Moon, J., Wetzel, A. W., Champion, A. S., Graham, B. J., Randlett, O., Plummer, G. S., Portugues, R., Bianco, I. H., Saalfeld, S., Baden, A. D., Lillaney, K., Burns, R., Vogelstein, J. T., Schier, A. F., Lee, W.-C. A., Jeong, W.-K., Lichtman, J. W., & Engert, F. (2017). Whole-brain serial-section electron microscopy in larval zebrafish. *Nature*, *545*, 345–349.

Hua, Y., Laserstein, P., & Helmstaedter, M. (2015). Large-volume en-bloc staining for electron microscopy-based connectomics. *Nature Communications*, *6*, 7923.

Insepov, Z., Yamada, I., & Sosnowski, M. (1998). Sputterring and smoothing of metal surface with energetic gas cluster beams. *Materials Chemistry and Physics*, *54*(1), 234–237. Symposium H of the 4th IUMRS International Conference in Asia.

Jia, W., Tchoudakov, R., Joseph, R., Narkis, M., & Siegmann, A. (2002). The conductivity behavior of multi-component epoxy, metal particle, carbon black, carbon fibril composites. *Journal of Applied Polymer Science*, *85*(8), 1706–1713.

Karnovsky, M. J. (1965). A formaldehyde-glutaraldehyde fixative of high osmolality for use in electron-microscopy. *Journal of Cell Biology*, *27*, 137–138.

Karnovsky, M. J. (1971). Use of ferrocyanide-reduced osmium tetroxide in electron microscopy. *Abstracts of the American Society for Cell Biology*, (p. 146).

Kasthuri, N., Hayworth, K., Berger, D., Schalek, R., Conchello, J., Knowles-Barley, S., Lee, D., Vázquez-Reina, A., Kaynig, V., Jones, T., Roberts, M., Morgan, J., Tapia, J., Seung, H., Roncal, W., Vogelstein, J., Burns, R., Sussman, D., Priebe, C., Pfister, H., & Lichtman, J. (2015). Saturated reconstruction of a volume of neocortex. *Cell*, *162*(3), 648–661.

Kinslow, R. (1970). *High-Velocity Impact Phenomena*. New York: Academic Press.

Knoll, M., & Ruska, E. (1932). Das elektronenmikroskop. *Zeitschrift für Physik*, *78*, 318–339.

Knott, G., Marchman, H., Wall, D., & Lich, B. (2008). Serial section scanning electron microscopy of adult brain tissue using focused ion beam milling. *Journal of Neuroscience*, *28(12)*, 2959–2964.

Kornfeld, J. (2017). *Connectomic analyses in the zebra finch brain*. PhD dissertation, Ruprecht-Karls-Universität.

Kornfeld, J., Benezra, S. E., Narayanan, R. T., Svara, F., Egger, R., Oberlaender, M., Denk, W., & Long, M. A. (2017). EM connectomics reveals axonal target variation in a sequence-generating network. *eLife*, *6*, e24364.

Kubota, Y., Sohn, J., Hatada, S., Schurr, M., Straehle, J., Gour, A., Neujahr, R., Miki, T., Mikula, S., & Kawaguchi, Y. (2018). A carbon nanotube tape for serial-section electron microscopy of brain ultrastructure. *Nat. Commun.*, *9*(1).

Lam, D., Enright, H. A., Cadena, J., Peters, S. K. G., Sales, A. P., Osburn, J. J., Soscia, D. A., Kulp, K. S., Wheeler, E. K., & Fischer, N. O. (2019). Tissue-specific extracellular matrix accelerates the formation of neural networks and communities in a neuron-glia co-culture on a multi-electrode array. *Scientific Reports*, *9*(1), 4159.

Langford, R. M. (2006). Focused ion beams techniques for nanomaterials characterization. *Microscopy Research and Technique*, *69*, 538–549.

Lee, E. H., Lewis, M. B., Blau, P. J., & Mansur, L. K. (1991). Improved surface properties of polymer materials by multiple ion beam treatment. *Journal of Materials Research*, *6*, 610–628.

Lichtman, J. W., & Denk, W. (2011). The big and the small: Challenges of imaging the brain's circuits. *Science*, *334*(6056), 618–623.

Lowe, D. G. (2004). Distinctive image features from scale-invariant keypoints. *International Journal of Computer Vision*, *60*(2), 91–110.

May, C. (1988). *Epoxy Resins. Chemistry and Technology*. New York: Marcel Dekker, Inc.

McDonald, K. (1984). Osmium ferricyanide fixation improves microfilament preservation and membrane visualization in a variety of animal cell types. *Journal of Ultrastructure Research*, *86*, 107–118.

Mikula, S., & Denk, W. (2015). High-resolution whole-brain staining for electron microscopic circuit reconstruction. *Nature Methods*, *12*, 541–546.

Mollenhauer, H. H. (1986). Surfactants as resin modifiers and their effect on sectioning. *Journal of Electron Microscopy Technique*, *3*(2), 217–222.

Moncrieff, D. A., Robinson, V. N. E., & Harris, L. B. (1978). Charge neutralisation of insulating surfaces in the SEM by gas ionisation. *Journal of Physics D: Applied Physics*, *11*(17), 2315.

Morgan, J. L., Berger, D. R., Wetzel, A. W., & Lichtman, J. W. (2016). The fuzzy logic of network connectivity in mouse visual thalamus. *Cell*, *165*(1), 192–206.

Pallotto, M., Watkins, P. V., Fubara, B., Singer, J. H., & Briggman, K. L. (2015). Extracellular space preservation aids the connectomic analysis of neural circuits. *eLife*, *4*, e08206.

Panegyres, K. P., & Panegyres, P. K. (2016). The Ancient Greek discovery of the nervous system: Alcmaeon, Praxagoras and Herophilus. *Journal of Clinical Neuroscience*, *29*, 21–24.

Purkinje, J. E. (1838). *Über Neuesten Untersuchungen aus der Nerven- und Hirn-Anatomie. (German) [New Investigations on Nerves and Brain]*. Prague: Gottlieb Haase.

Reimer, L. (1998). *Scanning Electron Microscopy: Physics of Image Formation and Microanalysis*. Berlin, Heidelberg: Springer.

Robinson, V. N. E. (1975). A wet stage modification to a scanning electron microscope. *Journal of Microscopy*, *103*(1), 71–77.

Sabatini, D. D., Bensch, K., , & Barrnett, R. J. (1963). The preservation of cellular ultrastructure and enzymatic activity by aldehyde fixation. *Cytochemistry and Electron Microscopy*, *17*, 19–58.

Sabu Thomas, R. T., Christophe Sinturel (2014). *Micro and Nanostructured Epoxy / Rubber Blends*. Weinheim: Wiley-VCH.

Scheffer, L. K., Xu, C. S., Januszewski, M., Lu, Z., Takemura, S.-y., Hayworth, K. J., Huang, G. B., Shinomiya, K., Maitlin-Shepard, J., Berg, S., Clements, J., Hubbard, P. M., Katz, W. T., Umayam, L., Zhao, T., Ackerman, D., Blakely, T., Bogovic, J., Dolafi, T., Kainmueller, D., Kawase, T., Khairy, K. A., Leavitt, L., Li, P. H., Lindsey, L., Neubarth, N., Olbris, D. J., Otsuna, H., Trautman, E. T., Ito, M., Bates, A. S., Goldammer, J., Wolff, T., Svirskas, R., Schlegel, P., Neace, E., Knecht, C. J., Alvarado, C. X., Bailey, D. A., Ballinger, S., Borycz, J. A., Canino, B. S., Cheatham, N., Cook, M., Dreher, M., Duclos, O., Eubanks, B., Fairbanks, K., Finley, S., Forknall, N., Francis, A., Hopkins, G. P., Joyce, E. M., Kim, S., Kirk, N. A., Kovalyak, J., Lauchie, S. A., Lohff, A., Maldonado, C., Manley, E. A., McLin, S., Mooney, C., Ndama, M., Ogundeyi, O., Okeoma, N., Ordish, C., Padilla, N., Patrick, C. M., Paterson, T., Phillips, E. E., Phillips, E. M., Rampally, N., Ribeiro, C., Robertson, M. K., Rymer, J. T., Ryan, S. M., Sammons, M., Scott, A. K., Scott, A. L., Shinomiya, A., Smith, C., Smith, K., Smith, N. L., Sobeski, M. A., Suleiman, A., Swift, J., Takemura, S., Talebi, I., Tarnogorska, D., Tenshaw, E., Tokhi, T., Walsh, J. J., Yang, T., Horne, J. A., Li, F., Parekh, R., Rivlin, P. K., Jayaraman, V., Costa, M., Jefferis, G. S., Ito, K., Saalfeld, S., George, R., Meinertzhagen, I. A., Rubin, G. M., Hess, H. F., Jain, V., & Plaza, S. M. (2020). A connectome and analysis of the adult *Drosophila* central brain. *eLife*, *9*, e57443.

Seligman, A. M., Wasserkrug, H. L., , & Hanker, J. S. (1966). A new staining method (OTO) for enhancing contrast of lipid–containing membranes and droplets in osmium tetroxide–fixed tissue with osmiophilic thiocarbohydrazide(TCH). *Journal of Cell Biology*, *30*, 424–432.

Song, K., Feng, Z., & Helmstaedter, M. (2022). High-contrast en-bloc staining of mouse whole-brain samples for em-based connectomics. *bioRxiv*.

Spurr, A. R. (1969). A low-viscosity epoxy resin embedding medium for electron microscopy. *Journal of Ultrastructure Research*, *26*(1), 31–43.

Svara, F. (2017). *Volume Electron Microscopic Analyses in the Larval Zebrafish*. PhD dissertation, Ruprecht-Karls-Universität.

Swanson, L., Newman, E., & Araque, A. (2017). *The Beautiful Brain: The Drawings of Santiago Ramon y Cajal*. United Kingdom: Abrams & Chronicle Books.

Templier, T. (2019). MagC, magnetic collection of ultrathin sections for volumetric correlative light and electron microscopy. *eLife*, *8*, e45696.

Titze, B., Genoud, C., & Friedrich, R. W. (2018). SBEMimage: Versatile acquisition control software for serial block-face electron microscopy. *Frontiers in Neural Circuits*, *12*.

Tomassy, G. S., Berger, D. R., Chen, H.-H., Kasthuri, N., Hayworth, K. J., Vercelli, A., Seung, H. S., Lichtman, J. W., & Arlotta, P. (2014). Distinct profiles of myelin distribution along single axons of pyramidal neurons in the neocortex. *Science*, *344*(6181), 319–324.

von Ardenne, M. (1938). Das elektronen-rastermikroskop. *Zeitschrift für Physik*, *109*, 553–572.

Walton, J. (1979). Lead aspartate, an en bloc contrast stain particularly useful for ultrastructural enzymology. *Journal of Histochemistry and Cytochemistry*, *10*, 1337–1342.

White, J. G., Southgate, E., Thomson, J. N., & Brenner, S. (1986). The structure of the nervous system of the nematode caenorhabditis elegans. *Philosophical Transactions of the Royal Society of London. Series B, Biological Sciences*, *134*, 1–340.

Yamada, I. (2016). *Materials Processing By Cluster Ion Beams: History, Technology, and Application*. Boca Raton: CRC Press.

Zheng, Z., Lauritzen, S., Perlman, E., Robinson, C. G., Nichols, M., Milkie, D., Torrens, O., Price, J., Fisher, C. B., Sharifi, N., Calle-Schuler, S. A., Kmecova, L., Ali, I. J., Karsh, B., Trautman, E. T., Bogovic, J. A., Hanslovsky, P., Jefferis, G. S., Kazhdan,

M., Khairy, K., Saalfeld, S., Fetter, R. D., & Bock, D. D. (2018). A complete electron microscopy volume of the brain of adult drosophila melanogaster. *Cell*, *174*, 730–743.

Acknowledgement

especially my cousin Liza for always being around and providing mental health breaks. I am deeply indebted to my best friend and husband, Edward, who was there every moment of this thesis and motivated me not to give up. Many thanks should also go to the Wall family for the fun holiday times together and the support.